

Integrated Optoelectronics Using Injection-Locked Vertical Cavity Surface Emitting Lasers

Final Report

Prepared For:

Army Research Office

Contract No. DAAH04-96-C-0038

Prepared By:

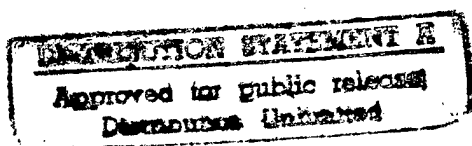
T.B. Simpson

JAYCOR, P.O. Box 85154, San Diego, California 92186-5154

and

J.M. Liu

Department of Electrical Engineering, University of California, Los Angeles
Los Angeles, California 90024-159410



March 10, 1997

19970515 042

REPORT DOCUMENTATION PAGE

Form Approved
OMB No. 0704-0188

Public reporting burden for this collection of information is estimated to average 1 hour per response, including the time for reviewing instructions, searching existing data sources, gathering and maintaining the data needed, and completing and reviewing the collection of information. Send comments regarding this burden estimate or any other aspect of this collection of information, including suggestions for reducing this burden, to Washington Headquarters Services, Directorate for Information Operations and Reports, 1215 Jefferson Davis Highway, Suite 1204, Arlington, VA 22202-4302, and to the Office of Management and Budget, Paperwork Reduction Project (0704-0188), Washington, DC 20503.

1. AGENCY USE ONLY (Leave blank)	2. REPORT DATE	3. REPORT TYPE AND DATES COVERED	
	3/10/97	Final Technical Rpt. 5/15/96 - 11/14/96	
4. TITLE AND SUBTITLE		5. FUNDING NUMBERS	
Integrated Optoelectronics Using Injection - Locked Vertical Cavity Surface Emitting Lasers		DAAH04-96-C-0038	
6. AUTHOR(S)			
Dr. Tom B. Simpson			
7. PERFORMING ORGANIZATION NAME(S) AND ADDRESS(ES)		8. PERFORMING ORGANIZATION REPORT NUMBER	
JAYCOR 9775 Towne Centre Drive San Diego, Ca 92121		NONE	
9. SPONSORING/MONITORING AGENCY NAME(S) AND ADDRESS(ES)		10. SPONSORING/MONITORING AGENCY REPORT NUMBER	
U.S. Army Research Office P.O. Box 12211 Research Triangle Park, NC 27709-2211		ARO 35762.1-EL-SBT	
11. SUPPLEMENTARY NOTES The views, opinions and/or findings contained in this report are those of the author(s) and should not be construed as an official Department of the Army position, policy, or decision, unless so designated by other documentation.			
12a. DISTRIBUTION/AVAILABILITY STATEMENT		12b. DISTRIBUTION CODE	
NOTE 1: Approval for public release; distribution unlimited			
13. ABSTRACT (Maximum 200 words)			
<p>This Final Report, describes experimental, analytical and numerical investigations of injection locking in a vertical cavity surface emitting laser for applications which benefit from optical control of microwaves. It concentrates on strong injection locking, where the imposition of the external optical signal not only locks the slave laser to the injected signal but also modifies the dynamic characteristics of the coupling between the optical field and the gain medium. This can lead to unstable dynamics in a vertical cavity surface emitting laser, or other semiconductor laser, and the optical output can consist principally of two frequency components. The frequency separation between these two components can be tuned across a broad range. We have found that a conventional coupled-equation model identifies all of the key phenomena that we observe in our data. Our data shows the particular laser that we studied had a very strong noise spectra and a polarization instability which would have kept it from many optical control of microwaves applications. However, these features are not intrinsic to vertical cavity surface emitting lasers. The ability to generate a tunable modulation with controlled output characteristics using such a compact optical source is very attractive. Further studies are required.</p>			
14. SUBJECT TERMS		15. NUMBER OF PAGES	
		16. PRICE CODE	
17. SECURITY CLASSIFICATION OF REPORT	18. SECURITY CLASSIFICATION OF THIS PAGE	19. SECURITY CLASSIFICATION OF ABSTRACT	20. LIMITATION OF ABSTRACT
UNCLASSIFIED	UNCLASSIFIED	UNCLASSIFIED	UL

Contents

1. INTRODUCTION	1
2. COUPLED EQUATION MODEL	4
3. EXPERIMENTAL APPARATUS	4
4. SEMICONDUCTOR LASER ABOVE THRESHOLD	8
4.1 Nonlinear Dynamics	11
4.2 Bandwidth Enhancement and Noise Analysis	17
4.3 VCSEL Characteristics	24
5. VCSEL NEAR THRESHOLD	27
6. VCSEL POLARIZATION AND NOISE CHARACTERISTICS	39
7. CONCLUSIONS AND ACKNOWLEDGMENTS	44

List of Figures

1	Transceiver concept using injection-locked semiconductor lasers.	2
2	Schematic diagram of the experimental apparatus.	5
3	Output power of the VCSEL under study.	7
4	Mapping of the locking and stability characteristics of the conventional, edge-emitting semiconductor laser.	9
5	Calculated eigenfrequency and measured frequency of the optical spectrum sideband peak for the conventional, edge-emitting semiconductor laser.	10
6	Measured optical spectra of the conventional, edge-emitting semiconductor laser with $\tilde{J} = 2/3$ under optical injection at the free-running optical frequency.	12
7	Measured optical spectra of the conventional, edge-emitting semiconductor laser with $\tilde{J} = 2/3$ under optical injection at a frequency offset ≈ 5.5 GHz.	14
8	Mapping of the experimentally observed dynamic regions for the conventional edge-emitting semiconductor laser.	16
9	Frequency pushing of the initially free-running spectral feature as a function of injection with the master laser frequency offset by 5.5 GHz.	18
10	Mapping of different characteristic operation regions of the laser under injection as a function of the injection parameter and the frequency detuning of the injection signal.	20
11	Resonance frequency of the laser under injection locking as a function of the injection parameter.	21
12	Total noise power of the laser under injection locking.	23
13	Measured optical spectra of the VCSEL with $\tilde{J} = 0.9$ under optical injection at the free-running frequency.	25
14	Variation of the resonance frequency of the VCSEL under external optical injection as a function of the square root of the injection power.	26
15	Measured optical spectra of the VCSEL with $\tilde{J} = 0.9$ as the injection frequency offset is shifted.	28
16	Measured optical spectra of a VCSEL as the bias current is varied.	30
17	Calculated optical spectra and histograms of the Fabry-Perot resonance frequency variation based on fluctuations in the carrier density.	31
18	Calculated optical spectra and histograms of the Fabry-Perot resonance frequency variation based on fluctuations in the carrier density.	32
19	Measured optical spectra of the VCSEL biased at 4.1 mA and subjected to external optical injection.	35
20	Calculated optical spectra of the VCSEL biased at 4.1 mA and subjected to external optical injection.	36
21	Spectra of the VCSEL under strong optical injection as the detuning is varied. . .	37
22	Measured pushing of the Fabry-Perot resonance as a function of the detuning of the injected signal.	38
23	Low-frequency power spectrum showing the resonance due to the antimode coupling between the two orthogonally polarized modes.	40

24	Optical spectra showing the effect of external optical injection on the two polarization components.	41
25	Optical spectra showing the effects of optical injection when the two polarization components are of similar magnitude.	42
26	Power spectrum at the beat frequency between the injection-locked optical signal component and the shifted Fabry-Perot cavity resonance feature for the laser under optical injection where the optical spectrum showed two strong optical components.	43

1. INTRODUCTION

The imposition of radio-frequency, microwave, or millimeter-wave (rfmm) modulations on optical carriers can be used for control of complex, high-frequency electronic systems. Transmission of the optical signals through fiber-optic links overcomes the losses and dispersion-induced distortion present in large bandwidth analog systems. However, the use of optical carriers for analog rfmm applications requires improvement in the performance of optical devices beyond what is currently available. Analog rfmm applications have stringent noise, dynamic range, and distortion specifications. They also require miniaturized components for practical implementation.

Semiconductor lasers have been the subject of considerable research and development activity over the past 30 years and now are used in a variety of applications including compact disc players and telecommunications. Research has continued to produce very small devices and over the past decade vertical cavity surface emitting lasers (VCSELs) have progressed from a laboratory curiosity to a commercial product. These laser cavities have dimensions of a few optical wavelengths, only a few micrometers on a side. They can be produced in two dimensional arrays on a single substrate. Recent reports have described modulation bandwidths in excess of 20 GHz. However, like any semiconductor laser, VCSELs have an intrinsic limit on the free-running modulation bandwidth and have relatively poor noise characteristics.

Our concept for the generation of tunable, coherent rfmm modulation of an optical carrier is based on bandwidth enhancement by injection of a near-resonant optical beam into a semiconductor laser. In recent work, we have established that the modulation bandwidth and broadband noise characteristics of a conventional, edge-emitting laser diode are significantly improved under appropriate injection by an optical beam [1, 2]. With optical injection by a stable laser diode, the bandwidth of a VCSEL, or other semiconductor laser, can be sufficiently enhanced to generate tunable modulation frequencies into the millimeter-wave regime. The enhancement is due not only to a power-enhanced carrier decay rate, the power increase can be small, but also to changes in the dynamic coupling between the carriers, gain medium, and the circulating optical field due to the optical injection. These changes provide the mechanism for precise frequency and phase control, as well as bandwidth enhancement. Significantly, the injected optical power required to induce these changes is only a few percent of the free-running output power of the laser. Because of their small size, low power requirements and surface-emitting geometry, VCSELs are useful for integration into near-monolithic optoelectronic circuits.

Injection locking of a semiconductor laser to a stable master laser allows one to tailor the response characteristics to emphasize a specific feature such as modulation bandwidth, flatness of response, or gain at a particular rfmm modulation frequency. This capability can be used to generate a wide variety of output characteristics with controlled amplitude and phase. A block diagram of a generic transceiver element built around an injection-locked laser diode is shown in Figure 1. The master laser is a stable, narrow-band laser oscillator which may have very poor high-frequency modulation characteristics. Between the master and slave laser, or multiple slave lasers, are optical elements which provide the proper coupling between the lasers and external signals and minimize unwanted feedback. The transceiver can be operated in the transmit mode where an electronic signal can be added to the bias current of the slave laser to produce an analog or digital modulation signal. Because the slave laser is operated as an injection-locked oscillator, it can have relatively poor free-running noise characteristics to

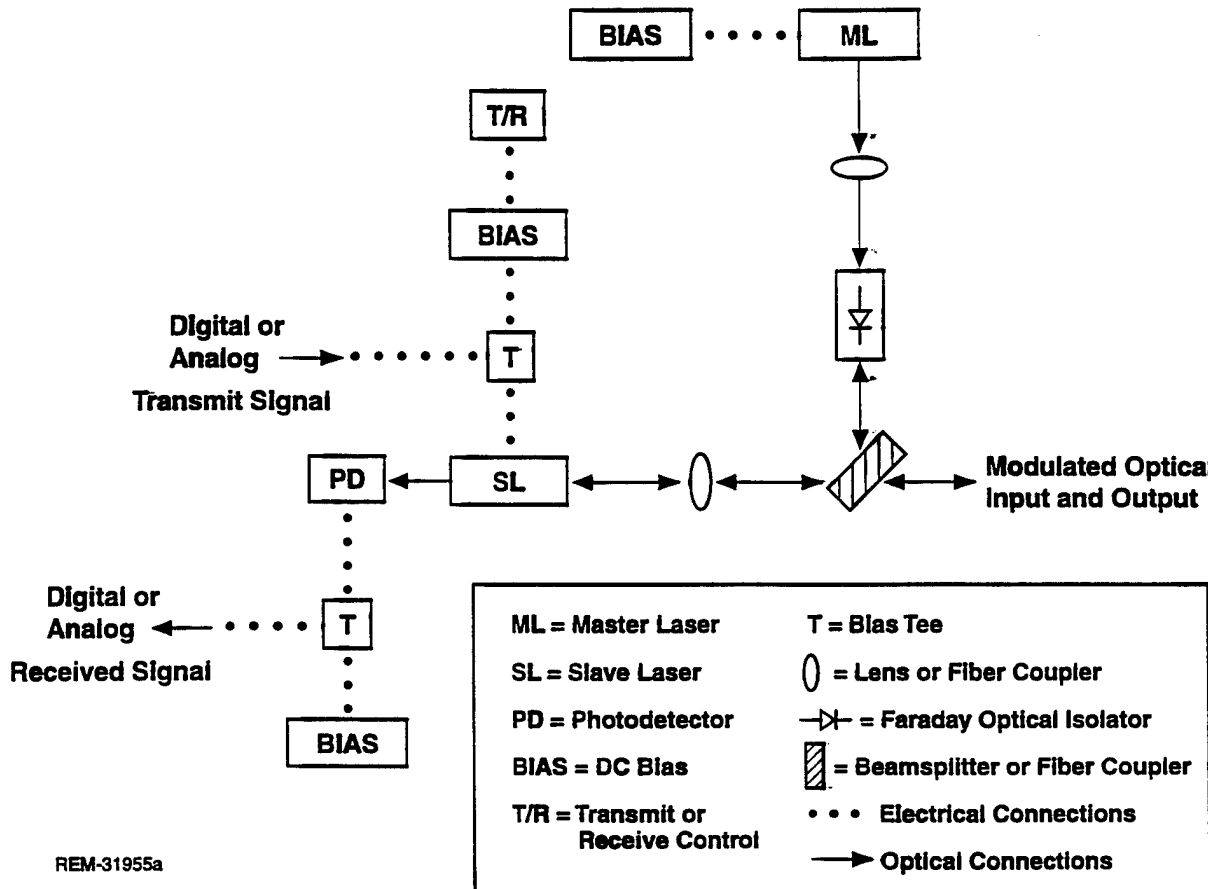


Figure 1: Transceiver concept using injection-locked semiconductor lasers.

emphasize high-frequency response. In the receive mode, the slave laser becomes a bandwidth tunable filter and preamplifier for modulated optical input to the photodetector. The master laser controls the central wavelength of the filter. By adjusting the bias of the slave laser, the bandwidth of the filter can be controlled. Because the master laser only has to inject a locking signal of a few percent of the power of the slave laser, a single master laser can control multiple transceiver elements. This feature should be quite useful for the coherent control of VCSEL arrays and for achieving the electrooptic integration needed for the control of complex rfmm electronics such as phased arrays. The optical elements necessary for the master/slave coupling can be miniaturized for use in waveguide and fiber-optic configurations. Bandwidth-enhanced VCSELs have the potential to be widely useful in applications where rfmm signals are usefully imposed on optical carriers.

This Phase I SBIR program had several key goals. First, we wished to verify that VCSELs showed the changes in their modulation characteristics that we had previously observed in conventional edge-emitting lasers. Second, we wished to verify that the model of semiconductor laser operation which we have developed identifies all the key phenomena in the output of injection-locked semiconductor lasers. This required that we compare our model calculations with results on both VCSELs and conventional edge-emitting lasers as we observed new phenomena during the course of this program. Finally, we wanted to investigate the noise characteristics of injection-locked VCSELs to see how their performance compared with the requirements of rfmm systems. As a result of our work, we are confident that our model has identified all the key phenomena of VCSELs under a strong injection-locking signal. We have found that the VCSEL which we have characterized displays the same kind of nonlinear dynamics, bandwidth enhancement and tunable modulation that we have observed in conventional, edge-emitting lasers. Our work has shown, however, that the VCSEL which we characterized tended to be quite noisy and that its range of operation was limited by polarization instabilities and by the appearance of multiple transverse modes at high bias currents. These features would limit the potential of VCSELs in rfmm applications. However, recently published work in the literature indicates that the ongoing research on the fabrication of VCSELs is improving their characteristics.

This report summarizes our findings. In the next section, we review the model of a semiconductor laser subject to a strong locking signal. This is followed by descriptions of our experimental apparatus and some general features of the specific VCSEL under investigation. Because nonlinear dynamics plays a critical role in the understanding of the semiconductor laser under strong optical injection, we then discuss a detailed mapping of the kinds of output dynamics that we observe under external optical injection and show that the VCSEL reproduces the kinds of dynamics that we observe in conventional edge-emitting lasers. Next we discuss some interesting features of the VCSEL which were not observed in our previous studies, with emphasis on VCSEL characteristics near threshold. There has been considerable controversy about the description of microcavity lasers, like VCSELs, near threshold. However, we show how our model recovers all of the novel features that we observe. Finally, we discuss noise characteristics of the modulation signals induced by the external optical injection and conclude with a brief discussion of possible future research that will be necessary to improve VCSEL performance for use in rfmm systems.

2. COUPLED EQUATION MODEL

Semiconductor lasers have been the subject of extensive modelling. They are an example of a class B laser system where the equation describing the polarization of the gain medium can be adiabatically eliminated due to the fast intraband carrier relaxation time [3]. This leaves two equations, one for the complex oscillating field within the laser cavity and one for the carrier density, to describe the dynamics of the single-mode laser under external optical injection [4, 5, 6].

$$\frac{dA}{dt} = -\frac{\gamma_c}{2}A + i(\omega_0 - \omega_c)A + \frac{\Gamma}{2}(1 - ib)gA + F + \eta A_i \exp(-i\Omega t), \quad (1)$$

$$\frac{dN}{dt} = \frac{J}{ed} - \gamma_s N - \frac{2\epsilon_0 n^2}{\hbar\omega_0} g|A|^2, \quad (2)$$

where A is the total complex intracavity field amplitude at the oscillation frequency ω_0 , γ_c is the cavity decay rate, and ω_c is the longitudinal mode frequency of the cold laser cavity. Γ is the confinement factor which gives the spatial overlap between the active gain volume and the optical mode volume, b is the linewidth enhancement factor which relates the dependence of the refractive index to changes in the gain, g . The gain is assumed to obey a linear dependence on changes in the carrier density, with coefficient g_N , and changes in the photon density, with coefficient g_p , about an appropriately chosen operating point [4]. N is the carrier density, J is the injection current density, e is the electronic charge, d is the active layer thickness, γ_s is the spontaneous carrier decay rate, and n is the refractive index of the semiconductor medium. Two source terms in the field equation are due to: 1) external optical injection with η being the coupling parameter, A_i the amplitude of the external field and Ω the offset frequency with respect to the free-running frequency of the injected laser, and 2) noise. F is the complex Langevin source term for the field noise due to spontaneous emission into the mode and external coupling out of the mode [7, 8].

$$\langle F(t) \rangle = 0 \quad (3)$$

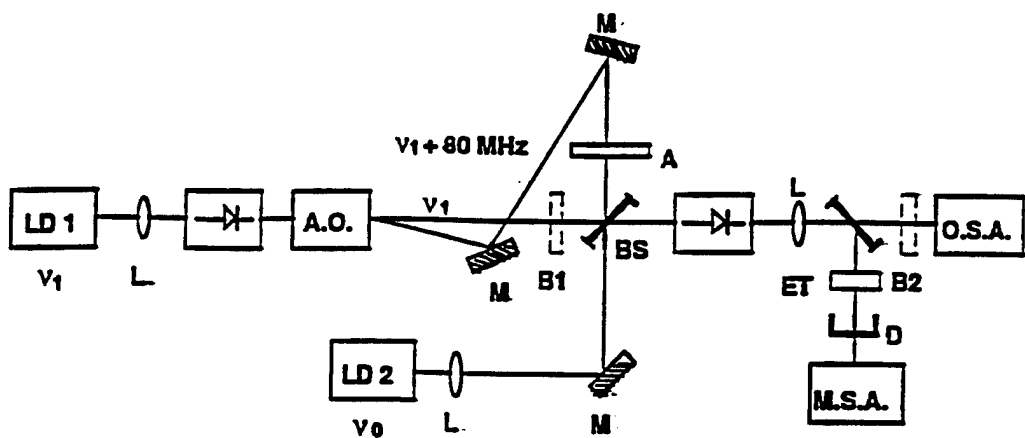
$$\langle F(t)F^*(t') \rangle = R_{sp}\delta(t - t') \quad (4)$$

$$\langle F(t)F(t') \rangle = 0 \quad (5)$$

where R_{sp} gives the strength of the field source term. The noise source terms in the carrier equation are omitted. They are relatively unimportant in determining the optical field spectra which we will emphasize.

3. EXPERIMENTAL APPARATUS

Figure 2 shows the experimental setup. The output of one laser diode (LD1) at a frequency ν_1 was passed through an acousto-optic modulator where a fraction, on the order of 10%, of the beam was deflected and shifted in frequency by 80 MHz. The shifted beam at $\nu_1 + 80$ MHz was used to probe a second laser (LD2) oscillating at $\nu_0 = \omega_0/2\pi$. Thus the frequency offset $f = \Omega/2\pi$ is given by $\nu_0 + f = \nu_1 + 80$ MHz and can be varied by varying ν_1 . Both lasers were temperature and current stabilized. To bring them to near-degenerate operating frequencies, the temperature



LEGEND:

LD: laser diode	A: variable attenuator
L: lens	BS: beam splitter
→-: optical isolator	ET: etalon
A.O.: acoustooptic modulator	D: fast photodiode
M: mirror	M.S.A.: R/F-microwave spectrum analyzer
B: removable beam block	O.S.A.: optical spectrum analyzer

Figure 2: Schematic diagram of the experimental apparatus.

was adjusted for gross frequency changes and then the current was adjusted for fine tuning of the frequency offset f . Optical isolators were used to avoid mutual injection and to reject back-reflected light from any components in the optical path. The use of the acousto-optic modulator improved the optical isolation between the two lasers. It could be removed and the full output of LD1 could be directed toward LD2 when high injection levels were required. The output of the injected laser was monitored using both optical and microwave/radio-frequency spectrum analyzers to measure both the optical field and power spectra. The data presented here were taken using the optical spectrum analyzer. However, both spectra are necessary for the determination of key dynamic parameters required for the comparison of experimental data with numerical data [4]. Measuring both spectra simultaneously allowed us to distinguish between amplitude and phase modulations of the output of the injected laser. The optical spectrum was measured with a Newport SR-240C scanning Fabry-Perot which has a free spectral range of 2 THz and a finesse of approximately 50,000, giving an optical frequency resolution of about 40 MHz. The power spectrum was obtained by detecting the output of the injected laser with a fast photodiode of 7 GHz frequency response and displaying the photodiode signal on the spectrum analyzer. In this experiment, the beam block B2 was removed to allow optical spectrum measurement while the beam block B1 in the path of ν_1 was inserted to block off the master laser output at ν_1 from the detection system. This allowed the direct measurement of the output from the injected laser.

In the data presented here, two sets of master/injected laser combinations were used. The first set consisted of a New Focus Model 6226 tunable external cavity laser as the master laser and a VCSEL as the injected laser. Unfortunately, from the perspective of getting useful, quantitative results, the VCSEL had the habit of spontaneously changing its output characteristics, such as threshold current, output wavelength, and dynamic parameters, during the course of this research program. The source of this feature is not clear. Such behavior has not been reported in the literature, but, in private conversations, other experimentalists investigating VCSELs have observed such behavior. Throughout much of the program, and for most of the data presented in this report, the VCSEL had the characteristics described below. When the VCSEL changed, it could be recharacterized by our model with appropriate dynamic parameters. Initially, the VCSEL had a threshold for laser oscillation of approximately 3.9 mA and emission wavelength of approximately 850 nm [9, 10, 11]. The total output power as a function of bias current is shown in Figure 3. At currents under approximately 6 mA, the VCSEL oscillates in the lowest order spatial mode but, due to the symmetry of the device, can emit in two orthogonally polarized modes. Also shown in Figure 3 is the polarized output power as a function of the injection current. The higher threshold polarization component eventually dominates the output and, when the output starts to be divided among several spatial modes, all show this polarization. The laser operated with these characteristics during the period that the threshold data and the polarization switching data that are presented later were taken. The dynamic characteristics of the laser were reported in Ref. [11]. More recently, the laser operated with a threshold of approximately 3.2 mA. Among the dynamic parameters the most notable change was the linewidth enhancement factor which was reduced from approximately 5-6 to 2-3. The data describing operation above threshold and showing the locking/unlocking bistability were taken with these characteristics.

The second master/slave combination consisted of two Spectra Diode Labs SDL-5301-G1 single-longitudinal and transverse mode GaAs/AlGaAs quantum-well lasers operating at 827.6 nm. These lasers are conventional Fabry-Perot edge-emitting lasers with one facet coated

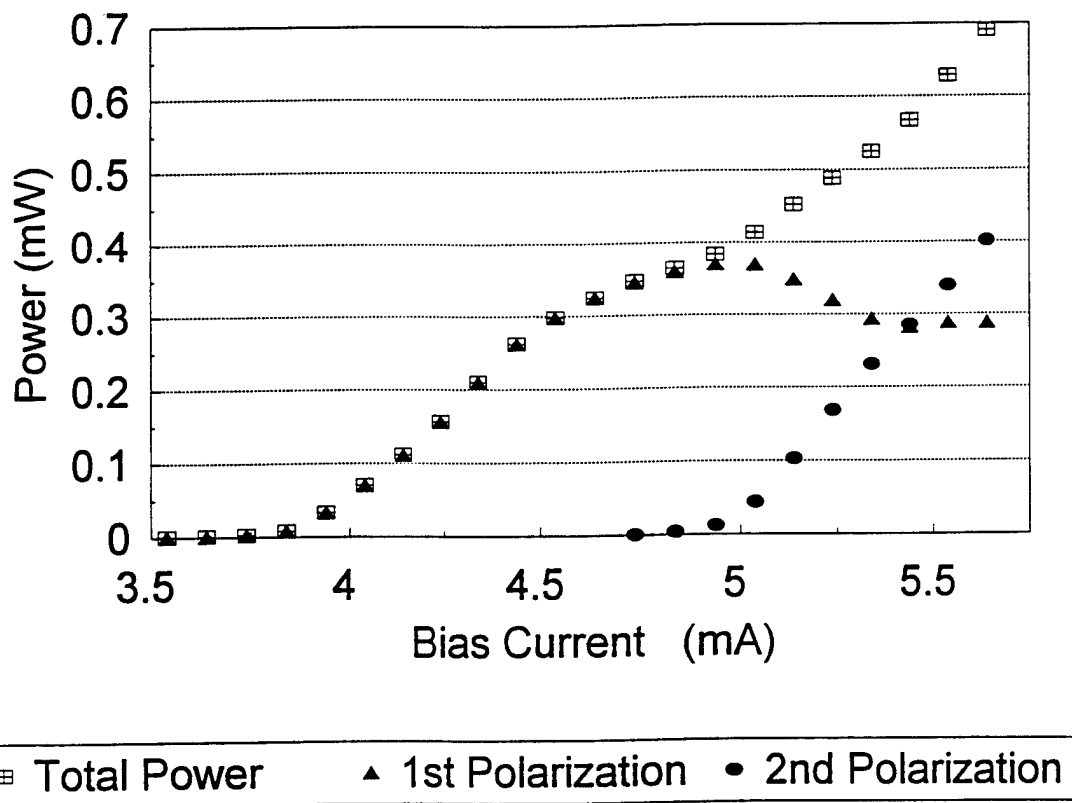


Figure 3: Output power of the VCSEL under study at bias currents where the output power is in one spatial mode with two orthogonal polarization modes.

for high reflection and the output facet coated for a reflection of a few percent. The threshold current for the injected laser was approximately 24 mA and the data presented here were taken at an injection current level of 40 mA. The master laser was operated at a higher current level, approximately 55-65 mA, to have lower noise characteristics.

4. SEMICONDUCTOR LASER ABOVE THRESHOLD

When a semiconductor laser is subjected to injection by a near-resonant external optical field, the laser output will exhibit a variety of optical spectra. By comparison between the experimentally observed spectra and calculated spectra, we have been able to categorize the dynamics. When the laser is biased well above threshold, the steady-state, free-running operating condition is used as the reference point for the gain in the calculations. The field amplitude and cavity density variations are normalized with respect to the steady-state optical field, A_0 , and carrier density, N_0 , respectively. The equations can then be rewritten as three coupled real equations for the normalized field, a , optical phase, ϕ , and normalized carrier density, \tilde{n} , in a form which shows explicitly the dependence on specific laser parameters which can be experimentally determined in the weak injection limit [12]:

$$\frac{da}{dt} = \frac{1}{2} \left[\frac{\gamma_n \gamma_c}{\gamma_s \tilde{J}} \tilde{n} - \gamma_p (2a + a^2) \right] (1 + a) + \gamma_c \xi \cos(\Omega t + \phi) + F' / |A_0|, \quad (6)$$

$$\frac{d\phi}{dt} = -\frac{b}{2} \left[\frac{\gamma_n \gamma_c}{\gamma_s \tilde{J}} \tilde{n} - \gamma_p (2a + a^2) \right] - \frac{\gamma_c \xi \sin(\Omega t + \phi) - F'' / |A_0|}{1 + a}, \quad (7)$$

$$\frac{d\tilde{n}}{dt} = -[\gamma_s + \gamma_n (1 + a)^2] \tilde{n} - \gamma_s \tilde{J} \left[1 - \frac{\gamma_p}{\gamma_c} (1 + a)^2 \right] (2a + a^2). \quad (8)$$

Here, $a = (|A| - |A_0|) / |A_0|$, ϕ is the phase difference between A and A_0 ; and $\tilde{n} = (N - N_0) / N_0$. The injection parameter, ξ , describing the external optical injection is defined as $\xi = \eta |A_0| / \gamma_c |A_0|$ and the injected power is proportional to ξ^2 . The decay rates γ_n and γ_p are the differential stimulated emission rate and gain saturation rates, formed from the steady state photon density and g_N and g_p , respectively [4]. $\tilde{J} = (J / ed - \gamma_s N_0) / \gamma_s N_0$, where J / ed is the carrier density injection rate. All input parameters required to numerically solve the set of coupled differential equations for a , ϕ and \tilde{n} can be determined experimentally [4]. After numerically integrating the normalized, coupled equations, the resulting time series are Fourier transformed to calculate the spectra.

Some key features can be predicted from a perturbation analysis with the set of coupled equations which assumes that the changes to the amplitude, phase and carrier density are sufficiently small that the three equations can be linearized. Figure 4 shows a typical mapping of the predicted locking and stability range based on a linearized analysis [2]. The actual values used to calculate the map correspond to the injected SDL laser at the bias current of 40 mA, $\tilde{J} = 2/3$, but the qualitative characteristics are more general. The analysis predicts an asymmetric locking range [13] with a bounded range of unstable operation within the locking range. The circulating field amplitude increases with increasing injection parameter and/or decreasing offset frequency within the locked region. A larger value of b increases the low frequency boundary of the locked

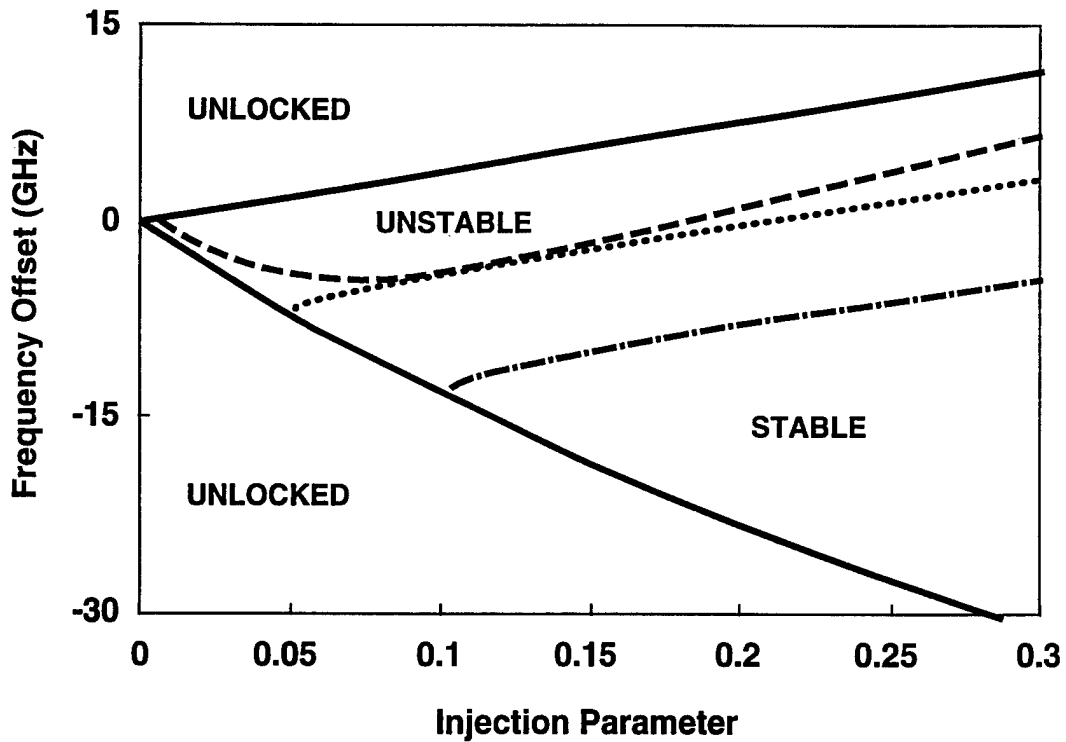


Figure 4: Mapping of the locking and stability characteristics of the conventional, edge-emitting semiconductor laser with $\tilde{J} = 2/3$ as a function of the frequency offset between the locking and free-running laser fields and the injection parameter, ξ . The thick solid line is the boundary of the injection-locked region. Shown in the interior of the locking region is the Hopf bifurcation line (thick dashed line) separating the stable and unstable operating regimes. The positive frequency boundary of the locked region is a line of constant output field amplitude at the free-running level, A_0 . Also shown are the lines for $1.1A_0$ (dotted) and $1.2A_0$ (dot-dashed).

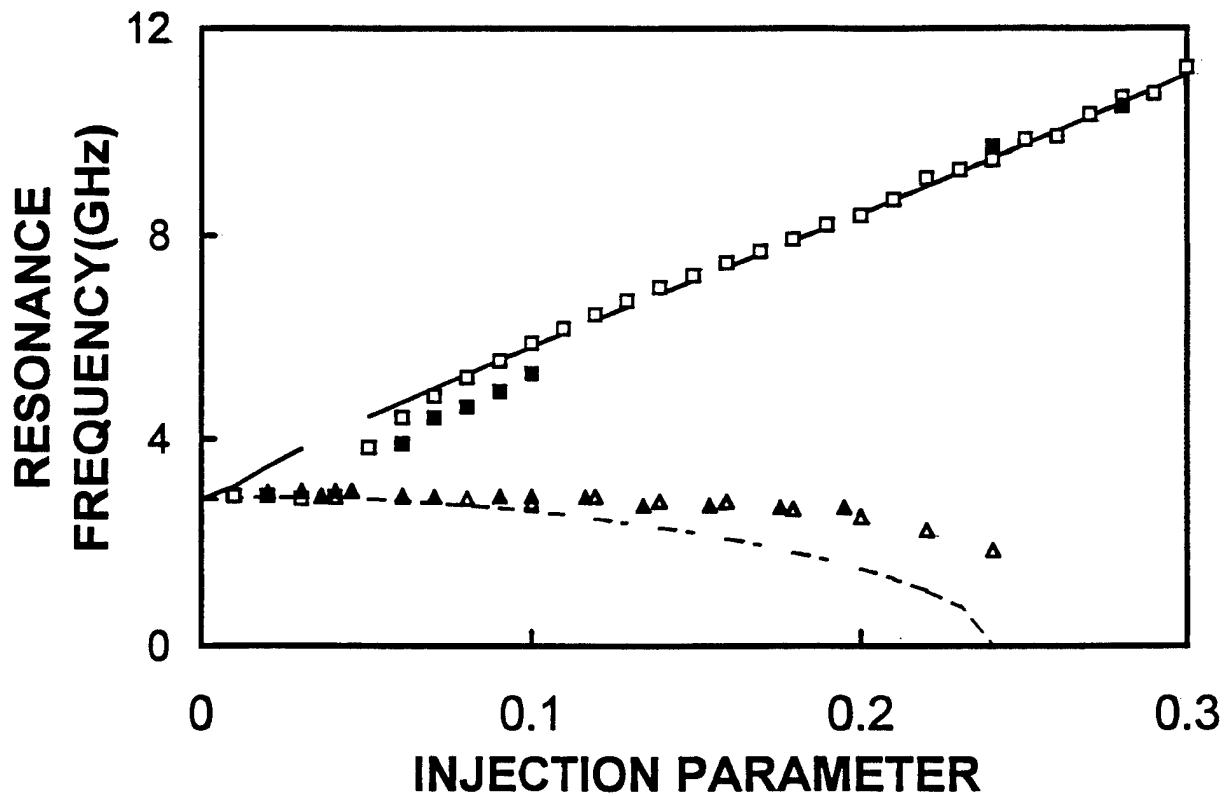


Figure 5: Calculated eigenfrequency and measured frequency of the optical spectrum sideband peak for the conventional, edge-emitting semiconductor laser with $\tilde{J} = 2/3$ as a function of the injection parameter, ξ . Two cases are plotted: Solid Line and Squares - injection at the free-running optical frequency, Dashed Line and Triangles - injection corresponding to $\phi_L = 0$. The former case shows unstable operation for $0.007 < \xi < 0.24$ while the latter case is always stable.

operating range and increases the range of unstable dynamics. A larger value of \tilde{J} shifts the unstable region to larger values of ξ with the low ξ limit shifting approximately in proportion to \tilde{J} or A_0^2 and the upper limit shifting approximately with A_0 [2]. The analysis also predicts that the eigenvalues of the coupled equations are strong functions of the operating point. Figure 5 plots the eigenvalues, or resonance frequencies of the field-free carrier coupling, as a function of ξ for two different cases. The first case is for external optical injection at the free-running frequency of the injected laser. This corresponds to a phase offset of $\arctan b$ between the master and injected laser optical fields in the linearized analysis. For this case the resonance frequencies increase monotonically with ξ . In contrast, when the injection frequency is changed as ξ is increased so that there is no phase offset between the master and injected laser optical fields, a case which approximately corresponds to following the low frequency boundary of the locked operating region, the linearized analysis predicts a decreasing resonance frequency. Also shown in Figure 5 are the resonance frequencies calculated by numerically integrating the full nonlinear equations and Fourier transforming the resulting time series and the experimentally measured resonance frequencies. The experimental data will be discussed below.

4.1 Nonlinear Dynamics

Using equations 6 to 8 with experimentally determined parameters, we have been able to produce calculated spectra quite similar to the observed spectra. When the noise source is eliminated from the calculated spectra, the spectra can be directly related to the underlying dynamics induced by the optical injection [6, 12, 14]. As an example, Figure 6 shows the progression of observed spectra from the conventional, edge-emitting laser when subjected to resonant, $\Omega = 0$, optical injection as the injection parameter, ξ , is increased. To determine the injection level, we calibrated the system by measuring the four-wave mixing spectrum in the weak injection limit and used our previously developed techniques to compare the generated sideband signal with the central peak [4]. The injected power was varied by changing the attenuation in the path of the master laser and the power level was monitored. In the spectra, the frequency is relative to the free-running frequency or, equivalently, the injection frequency and the scale of the signal level is consistent throughout the series. Expanded versions of the spectra showing weak details are referenced to the right vertical axis scale. Figure 6(a) is the free-running spectrum consisting of a single peak and weak relaxation resonance sidebands which are visible in the expanded scale version of the spectrum. The asymmetry is due to b . In Figure 6(b) $\xi^2 = 1 \times 10^{-4}$, and the spectrum consists of relatively narrow peaks separated by a frequency spacing of 2.9 GHz, which is the relaxation resonance frequency of the free-running laser. These are typical features of highly unstable injection locking [13]. In Figure 6(c) $\xi^2 = 3 \times 10^{-4}$, broad period-doubling features appear in the spectrum between the narrow oscillation peaks [12]. They are stronger at negative detunings, a reflection of the positive value of b . Comparing the expanded versions of (b) and (c) clearly shows the qualitative difference between the spectra before and after the period-doubling features emerge. The field noise source causes the broadening of the period-doubling features. When it is removed in the calculated spectra, sharp period-doubling peaks result [12]. In Figure 6(d), $\xi^2 = 1.3 \times 10^{-3}$, the spectrum becomes dominated by a broad pedestal and many secondary peaks develop. Relatively little energy remains in the narrow injection spike. At this

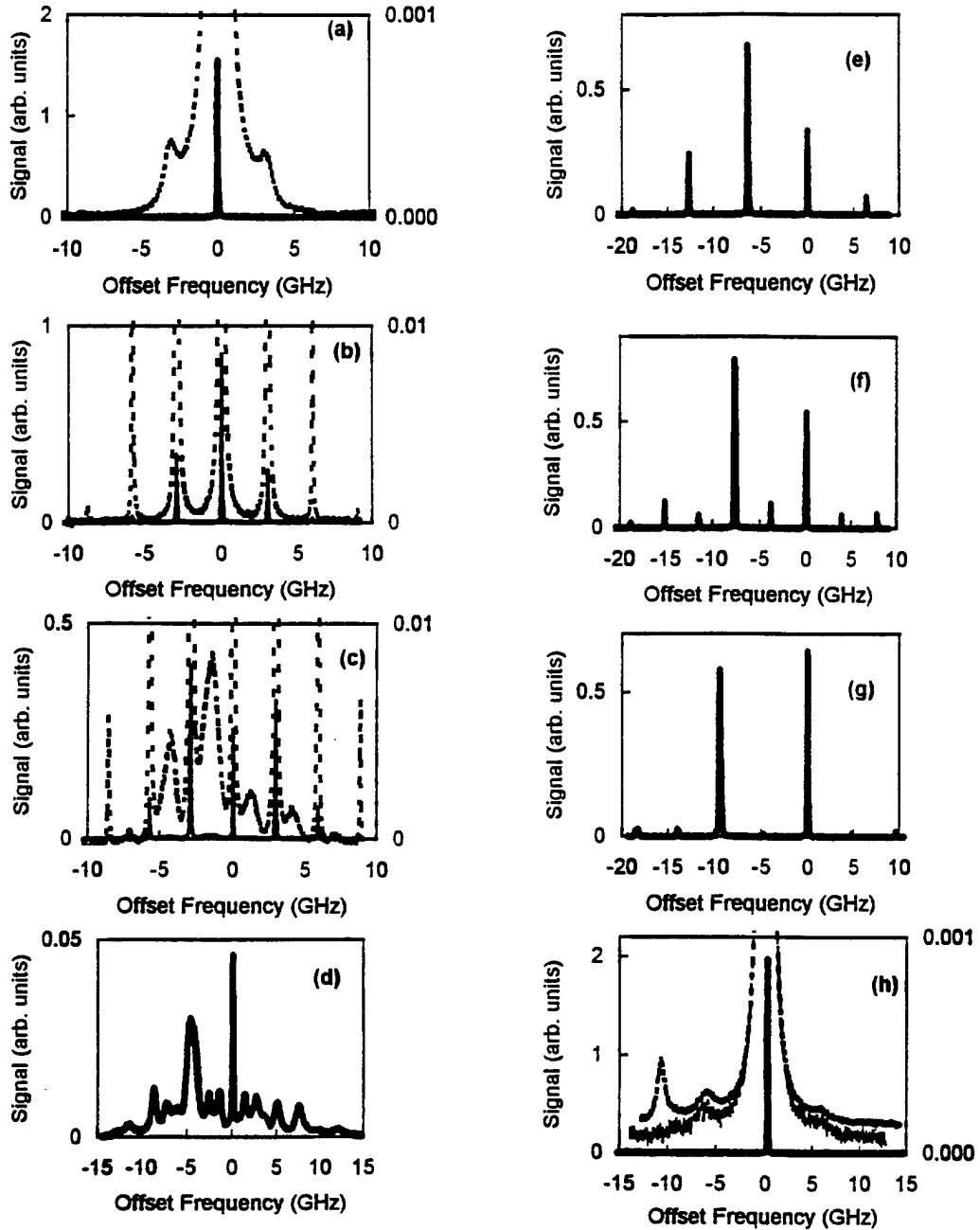


Figure 6: Measured optical spectra of the conventional, edge-emitting semiconductor laser with $\tilde{J} = 2/3$ under optical injection at the free-running optical frequency: (a) free-running operation with expanded scale showing the relaxation resonance sidebands, (b) unstable injection locking, limit cycle, at $\xi^2 = 1 \times 10^{-4}$ with expanded scale spectrum, (c) period doubling at $\xi^2 = 3 \times 10^{-4}$ with features shown clearly in the expanded scale, (d) chaotic dynamics at $\xi^2 = 1.3 \times 10^{-3}$, (e) limit cycle at $\xi^2 = 3.6 \times 10^{-3}$, (f) period doubling at $\xi^2 = 7.2 \times 10^{-3}$, (g) transition back to limit cycle at $\xi^2 = 1.7 \times 10^{-2}$, and (h) stable operation at $\xi^2 = 8.5 \times 10^{-2}$ along with expanded scale spectrum and the expanded scale sideband spectrum of the master laser.

stage chaos has fully developed and elimination of the noise source in the calculated spectra does not change the qualitative features [12]. Within the region of chaotic dynamics, a fraction of the oscillating power, increasing to up to 35% as the injection level is increased, is shifted from the principal oscillating mode into several of the weak side modes. Over a narrow injection range, the broadened spectrum collapses again into an equally spaced set of narrow features, as shown in Figure 6(e) where $\xi^2 = 3.6 \times 10^{-3}$, and the principal mode regains its full power [6]. Now, however, the separation of the peaks has increased and the spectrum is much more strongly shifted to the negative components. At still higher injection levels, Figure 6(f) where $\xi^2 = 7.2 \times 10^{-3}$, a new, clear period doubling is observed with a further increase of the peak separation and relative strengthening of the negative frequency components. The strongest spectral feature is clearly frequency-shifted, pushed by the resonant injection. The period doubling peaks then steadily decrease in amplitude as the resonance peak monotonically increases while the peak separation continues to increase. The spectra in Figure 6(g) is observed when $\xi^2 = 1.7 \times 10^{-2}$ and the injection peak again begins to dominate the spectrum. Eventually, the side peaks decrease in magnitude so that only a single peak at the injection frequency dominates the spectrum. In Figure 6(h) $\xi^2 = 8.5 \times 10^{-2}$ and stable dynamics has been reestablished. The peak separation has now increased to 10.5 GHz and the side peak is visible in the expanded spectrum. Also visible in the expanded spectrum are replicas of the relaxation resonance features of the master laser. The identification of these features is confirmed by comparison with sideband spectrum of the master laser, also shown. At high injection levels, the noise sidebands of the master laser appear in the spectrum of the injection-locked slave. These noise features do not reflect the dynamics of the injected laser system. The dynamics are reflected in the shifted resonance feature. Note that the strong asymmetry of the resonance peaks continues when stable dynamics has been reestablished. The weak asymmetry in the resonance peaks of the free-running laser has become a strong asymmetry in the injection-locked laser. The measured shift in the resonance peaks is compared with the calculated eigenfrequencies of the coupled equations in Figure 5 and shows very good agreement with the full nonlinear calculation and reasonable agreement with the linearized treatment.

Before proceeding to a more general picture of the dynamics induced under external optical injection, we distinguish a special type of period-doubling-like spectra, the region of subharmonic resonance [15]. Here, the half offset frequency feature can totally dominate the frequency component offset from the central peak by the resonance frequency. Figure 7 shows a set of spectra which illustrate the subharmonic resonance. Again, the offset frequency is referenced to the frequency of the free-running laser. In these spectra the master laser is offset by ≈ 5.5 GHz and the injection level is varied. A complementary set of spectra, where the injection level is held constant while the offset frequency is varied from below to above twice the relaxation resonance frequency of the free-running laser, has been presented elsewhere [15]. At low injection levels the spectrum consists of narrow, weak sidebands, equally and oppositely offset from a main peak with its relaxation resonance sidebands, as shown in Figure 7(a). These narrow features are due to regenerative amplification of the injected signal and four-wave mixing between the injected signal and the central peak [4]. As the injected signal is increased, the spectral features near the relaxation resonance frequency narrow and increase, Figure 7(b) where the injection level is $\xi^2 = 2.1 \times 10^{-4}$. Note, however, that these features are halfway between the injection feature, or its oppositely shifted partner, and the central peak. This frequency is slightly less than the

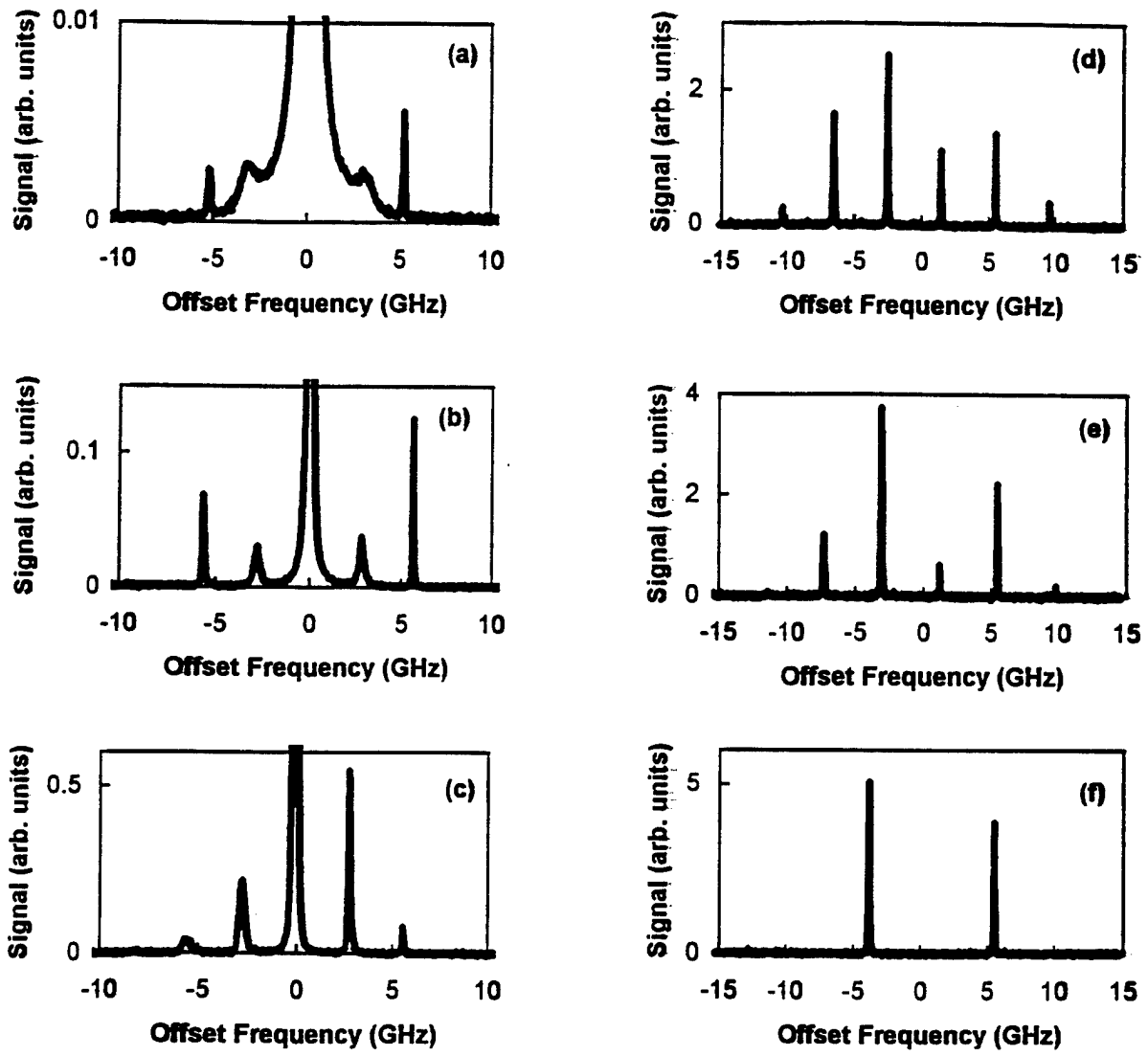


Figure 7: Measured optical spectra of the the conventional, edge-emitting semiconductor laser with $\tilde{J} = 2/3$ under optical injection at a frequency offset ≈ 5.5 GHz: (a) weak injection with regenerative amplification and four-wave mixing sidebands, (b) enhanced subharmonic signal at $\xi^2 = 2.1 \times 10^{-4}$, (c) subharmonic resonance at $\xi^2 = 4 \times 10^{-4}$, (d) weak period quadrupling at $\xi^2 = 2.6 \times 10^{-3}$, (e) period doubling at $\xi^2 = 6 \times 10^{-3}$, and (f) limit cycle at $\xi^2 = 1.2 \times 10^{-2}$.

relaxation resonance frequency of the free-running laser. There is also a small frequency pushing of the central peak. At still higher injection levels, Figure 7(c) with $\xi^2 = 4 \times 10^{-4}$, the subharmonic resonance nature of the dynamics becomes clear. The sideband at the injection frequency is now dominated by the feature at half the offset. Also, the frequency pushing has stopped and the central peak is slightly pulled toward the injected frequency [15]. As the injection level is increased to $\xi^2 = 2.6 \times 10^{-3}$, Figure 7(d), the pushing of the central peak and the dominance of the resonance frequency, now significantly larger than the initial offset frequency, are reestablished. This is actually a period-quadrupling spectrum, with weak, broadened features just discernible above the noise level in between the some of the sharp spectral features. At higher injection levels the spectrum follows the progression to period doubling, Figure 7(e) with $\xi^2 = 6 \times 10^{-3}$, and to limit cycle oscillations, Figure 7(f) with $\xi^2 = 1.2 \times 10^{-2}$. The frequency pushing continues to increase and the pushed feature gets relatively weaker. At very high injection levels, $\xi^2 > 3 - 4 \times 10^{-2}$, the laser output begins to smoothly shift to other longitudinal modes.

Using spectra like that of Figures 6 and 7, we have constructed a mapping of the dynamics for the laser at this pump level as the injection parameter and the frequency offset are varied. In the mapping of Figure 8, the frequency axis is relative to the free-running frequency of the injected laser. The map symbols are: 4 - perturbation spectrum with weak regenerative amplification and four-wave mixing sidebands; S - stable injection locking; SR - subharmonic resonance; P1 - limit cycle oscillation; P2 - period doubling; P4 - period quadrupling; Chaos - deterministic chaos; M' - multiwave mixing with most output on another longitudinal mode; hatched regions - principal output on another longitudinal mode; thin lines - smooth transition between dynamic regions; thick dotted lines - abrupt mode hop transitions with minor hysteresis; thick dashed lines with arrow - one way mode hops out of mode; thick solid lines - abrupt transition to/from a region of chaos or multiwave mixing where there is significant power in another longitudinal mode, from/to a region with power primarily in the principal mode. The smooth transitions represented by the thin lines are approximate. For instance, a peak-to-sideband ratio of 10:1 was used for the transition line from stable to unstable dynamics. For small values of ξ , the optical injection acts as a perturbation. Weak sidebands are generated at the offset frequency of the external optical injection and equally and oppositely shifted from the central peak. These are the regenerative amplification and four-wave mixing sidebands, respectively. As the injection parameter is increased, various dynamic instabilities develop. At negative detunings the locked region resembles the predictions of the mapping from the linearized analysis. There is a narrow region of stable injection locking at lower values of ξ which opens up for $\xi \gtrsim 0.1$.

Most of the dynamic regions and transitions are directly recovered in the single-mode model of semiconductor laser operation. The value of the linewidth enhancement factor, b , is a critical parameter in determining the limits of the range of nonlinear dynamics and whether that range will include regions of chaotic dynamics. From the mapping it can be seen that the second region of period-doubling dynamics along the $\Omega = 0$ line is associated with a second region of chaotic dynamics at positive offset frequencies. The positive detuning region is more complicated because boundaries between different types of nonlinear dynamics are difficult to draw. For instance, when the offset is approximately equal to the free-running relaxation resonance frequency, the distinction between the perturbation, four-wave-mixing-type, spectrum and the limit-cycle spectrum blurs into one of qualitative difference. There are no clear features in the

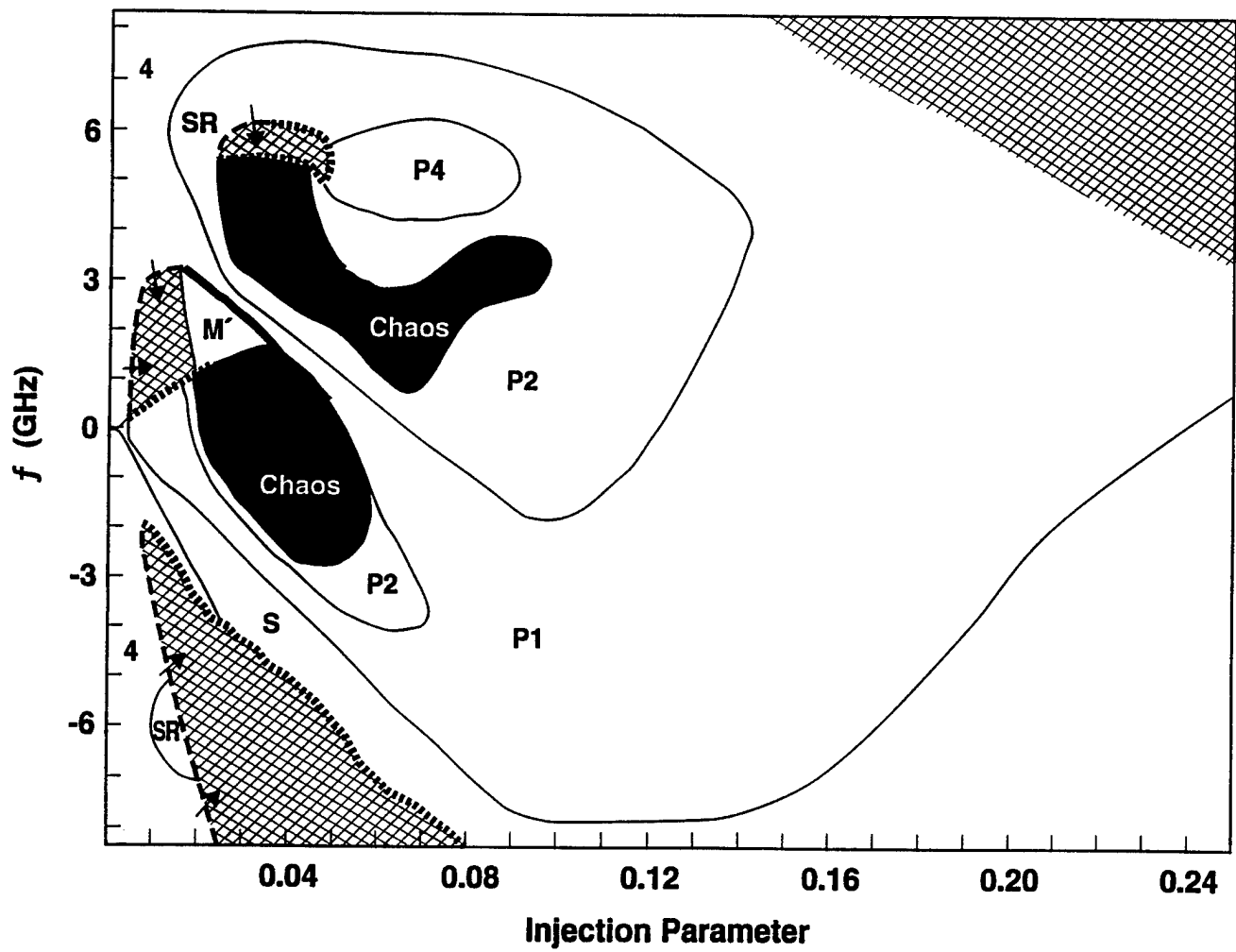


Figure 8: Mapping of the experimentally observed dynamic regions for a conventional edge-emitting semiconductor laser with $\tilde{J} = 2/3$. The dynamics are determined by comparison of observed spectra with calculated spectra with and without noise. Symbols are defined in the text.

spectra which distinguish between locked and unlocked operation. The various unstable dynamics show no qualitative distinction as they cross the line where the linearized analysis divides locked and unlocked operation. Within the nominally locked operating regime, the various spectral features of the optical spectrum clearly show broadening with respect to the narrow feature at the injection frequency and are, therefore, not locked to the injection source.

Also associated with injection at positive offset frequencies is the general trend of frequency pushing of the originally free-running spectral feature. One anomaly of the subharmonic resonance is the slight pulling of the original oscillation peak in that region. For optical injection at positive offset frequencies, the excitation has a tendency to push the original oscillation peak to negative offset frequencies with the degree of pushing increasing as the offset frequency of the excitation is decreased or the injection parameter is increased. Figure 9 plots the frequency pushing for the injection offset at 5.5 GHz. More details of the weak frequency-pulling effect around the subharmonic resonance are given elsewhere [15]. Here, we concentrate on the general frequency-pushing trend. The pushing effect highlights a key point which is central to the asymmetry of the mapping. The external optical injection shifts the Fabry-Perot oscillation frequency of the laser cavity by changing the steady-state carrier density. The excitation follows the new Fabry-Perot frequency along the zero phase offset line in the stable operating region. When the optical excitation is off of the Fabry-Perot resonance, there is a new frequency in the coupled field-carrier system. The shifting of the resonance oscillation frequency with excitation level is due to the competition between the original relaxation resonance, and its associated damping, and the frequency difference between the injected signal and this new resonance, and its associated phase offset, to control the response. The system restabilizes within the injection-locked operating region when the Fabry-Perot frequency shifts and associated damping are large compared to the original system resonances [2]. In this region of stable operation under strong injection, where linearized dynamics again prevail, the modulation characteristics of the semiconductor laser are strongly modified. Bandwidth enhancement, associated with the enhanced resonance frequencies, beyond the theoretical limit of the free-running laser is calculated to be achievable [2].

4.2 Bandwidth Enhancement and Noise Analysis

Many characteristics of a semiconductor laser can be modified by injection locking. Under weak injection locking, single-mode oscillation, frequency-chirp reduction [16], and linewidth improvement [17] in a laser can be realized. Under strong injection, the dynamic characteristics of a laser can be substantially changed. Our recent analysis [1, 2] has revealed that the modulation characteristics of a semiconductor laser can be significantly improved with strong injection locking under proper conditions. Using a tunable optical signal to probe a strongly injection-locked semiconductor laser, we have observed a parasitic-free intrinsic bandwidth that is beyond the K -factor limit and is more than three times the bandwidth of the laser in the free-running condition [18]. Besides bandwidth enhancement, our previous analysis also indicated that strong injection locking can lead to a broad-band reduction of the laser noise as well [1]. However, an enhancement in the modulation bandwidth is not necessarily accompanied by a reduction in the laser noise.

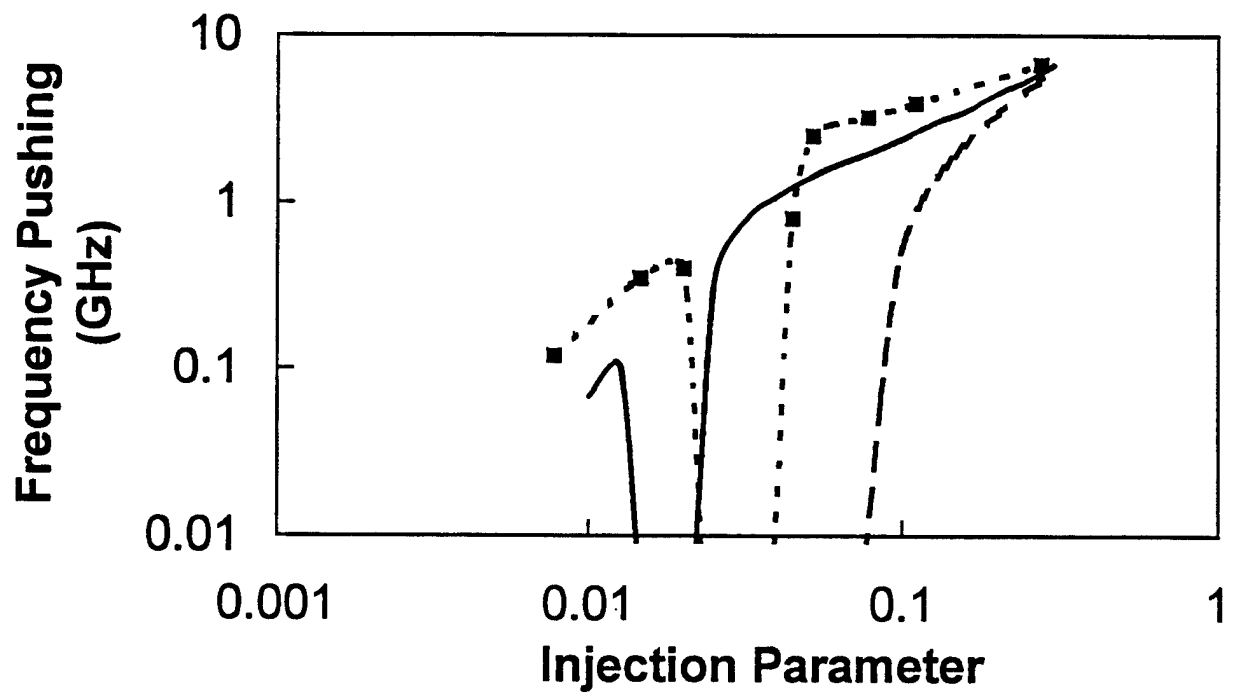


Figure 9: Frequency pushing of the initially free-running spectral feature as a function of injection with the master laser frequency offset by 5.5 GHz, experimental data - squares and dotted line, full nonlinear equations - solid line, eigenvalues of linearized equations - dashed line. Frequency pulling in the subharmonic resonance region causes the abrupt dip in the experimental data and nonlinear calculation curves.

Referring back to the bandwidth enhanced transceiver in Figure 1, the specific application will determine what properties of the semiconductor laser under optical injection need to be emphasized. To capitalize on the potential benefit of strong injection locking of a semiconductor laser for its practical application as a large-bandwidth, low-noise device, it is clearly necessary that conditions exist for bandwidth enhancement, noise reduction, and stable locking to be simultaneously achieved. Here, we quantify such conditions. It is well known that except for very weak injection, stable locking occurs predominantly with the frequency of the injection signal negatively detuned from the free-running oscillation frequency of the laser [19, 13]. However, even in the stable locking region, a locking-unlocking bistability has been observed above a certain injection level [20]. We use the conventional, edge-emitting laser as our model system. Because its parameters have been accurately determined, the simulation results agree exceedingly well with any experimental data that we have collected. In the cases where the linearized analytical model [2] applies, the analytical results are also shown for comparison.

We fix the current injection level at $\tilde{J} = 2/3$, which corresponds to an injection current level of 40 mA and a free-running output power of 9 mW. At this current level, the corresponding laser parameters that are used in our numerical and analytical calculations for the laser characteristics are $\gamma_c = 2.4 \times 10^{11} \text{ s}^{-1}$, $\gamma_s = 1.458 \times 10^9 \text{ s}^{-1}$, $\gamma_n = 1.34 \times 10^9 \text{ s}^{-1}$, $\gamma_p = 2.41 \times 10^9 \text{ s}^{-1}$, $b = 4$, and $R_{sp} = 4.7 \times 10^{18} \text{ V}^2 \text{m}^{-2} \text{s}^{-1}$. Meanwhile, at $\tilde{J} = 2/3$, the resonance frequency of this laser in the free-running condition is $f_r = 2.93 \text{ GHz}$. All of these parameters were determined experimentally [4].

At a given injection current level, the characteristics of a semiconductor laser subject to an external optical injection depend on two key parameters of the injection signal: the frequency detuning, $\Omega/2\pi$, of the injection signal with respect to the free-running frequency of the laser, and the injection parameter, ξ , that indicates the strength of the injection signal received by the laser. Figure 10 shows the mapping of different characteristic operation regions of the laser under injection as a function of these two parameters. In this figure, as well as in the two following figures, the thick solid curves are obtained from the linearized analytical solution whereas the open symbols represent data obtained from numerical simulation using the full nonlinear model. The thick broken curves are merely guides of the eye.

The locking region shown in Figure 10 is asymmetric with respect to the zero frequency detuning and opens up significantly at high injection levels. Curve *a* is the Hopf bifurcation boundary above which the laser becomes unstable though it may be locked. Curve *e* is the boundary below which the laser cannot be locked. The region between curves *c* and *e* is the locking-unlocking bistability region. Note that the locking-unlocking bistability does not occur at an injection level lower than $\xi = 0.06$ or at a detuning less negative than -8 GHz . In this bistability region, the laser can be either locked or unlocked, depending on the initial condition. If a laser is initially injection-locked with a set of parameters in the stable locking region between curves *a* and *c*, it remains locked while the injection signal is slowly tuned in frequency or in strength to cross the boundary marked by curve *c* into the bistability region. Conversely, if it is initially unlocked, it remains unlocked while the injection signal is tuned within the bistability region until curve *c* is crossed to enter the stable locking region when the laser suddenly becomes locked. Therefore, unconditionally stable locking occurs only in the region between curves *a* and *c*.

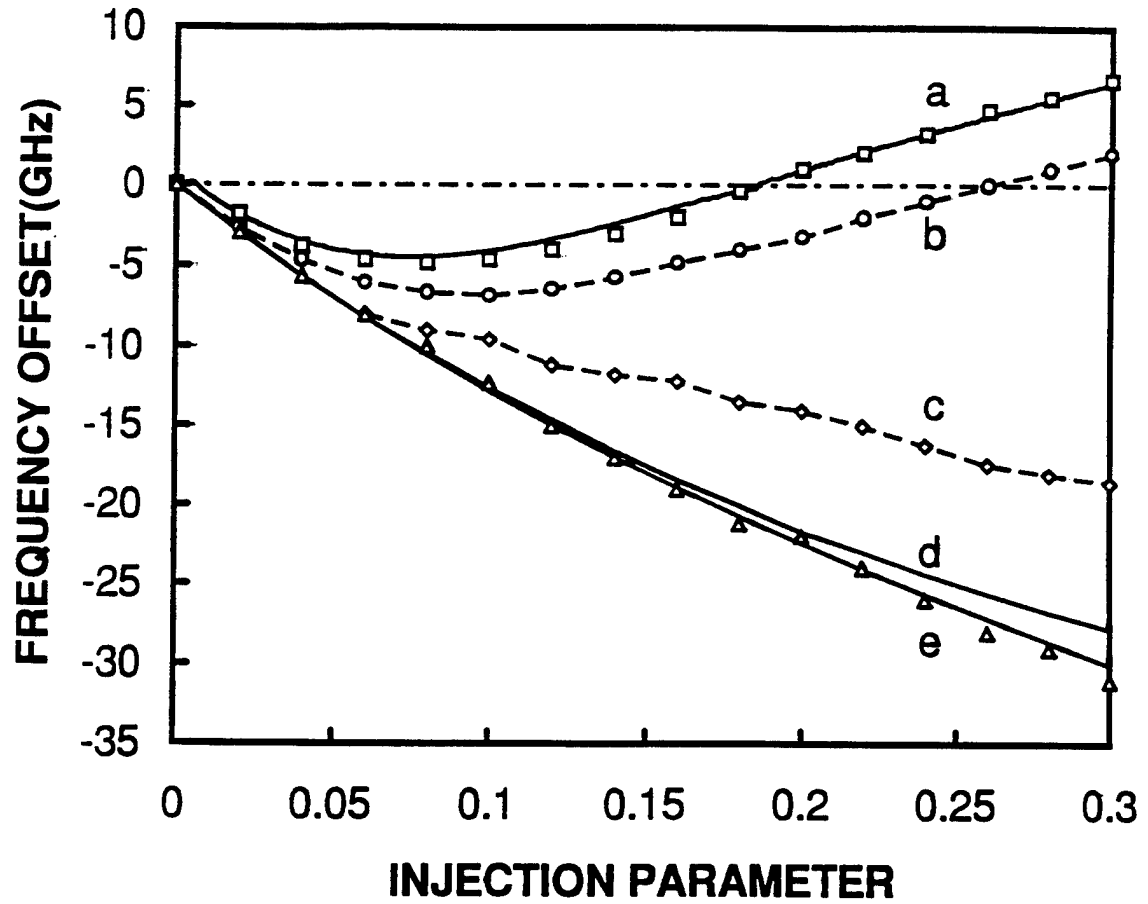


Figure 10: Mapping of different characteristic operation regions of the laser under injection as a function of the injection parameter and the frequency detuning of the injection signal. The thick solid curves are obtained from the linearized analytical solution while the open symbols are data obtained from numerical simulation using the full nonlinear model. The thick broken curves are merely guides of the eye. Curve *a* is the Hopf bifurcation boundary below which the laser is stably locked. Noise reduction under injection locking is found in the region below curve *b*. A locking-unlocking bistability is observed in the region bounded by curves *c* and *e*. Bandwidth enhancement under injection locking occurs in the region above curve *d*. The laser cannot be locked in the region below curve *e*.

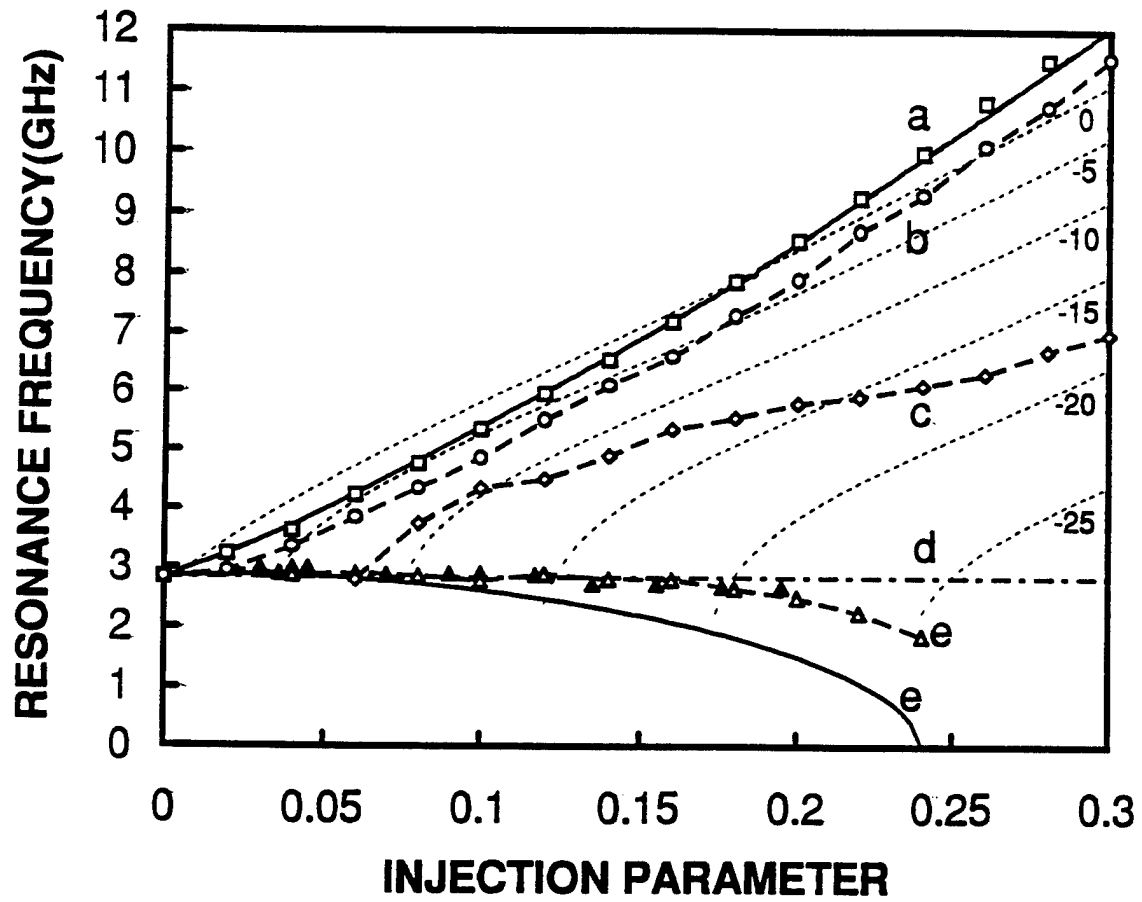


Figure 11: Resonance frequency of the laser under injection locking as a function of the injection parameter. Line d marks the resonance frequency $f_r = 2.93$ GHz for the laser in the free-running condition. Each of the thick curves corresponds directly to the curve that has the same label in Figure 10. The open symbols are data obtained from numerical simulation using the full nonlinear model. The closed triangles are experimental data taken under the conditions on curve e of Figure 10. The thin dotted curves are contour curves for fixed values of frequency detuning in gigahertz.

Figure 11 shows the resonance frequency of the laser under injection locking as a function of the injection parameter. Line *d* marks the resonance frequency $f_r = 2.93$ GHz for the laser in the free-running condition. Each of the thick curves corresponds directly to the curve that has the same label in Figure 10. For example, curve *a* in Figure 11 shows how the resonance frequency of the laser under injection locking varies along the Hopf bifurcation boundary and curve *c* shows how it varies along the bistability boundary. The thin dotted curves in Figure 11 are contour curves for fixed values of frequency detuning. They show how the resonance frequency varies with the injection parameter when the frequency detuning is fixed at a certain value in gigahertz that labels a curve.

While not a precise correlation, the resonance frequency is often a good indicator of the modulation bandwidth. From Figure 11, we find that bandwidth enhancement due to injection locking occurs within almost the entire locking region of interest shown in Figure 10. Only in a very narrow range between curves *d* and *e* within the bistability region does injection locking not lead to bandwidth enhancement. Most significant is the fact that bandwidth enhancement does occur in the entire stable locking region between curves *a* and *c*. In fact, it can be seen from Figure 11 that substantial bandwidth enhancement can be realized anywhere in the stable locking region for $\xi > 0.1$. Along the lower boundary of the locking region marked by curve *e*, the experimentally observed resonance frequencies, which are confirmed by the simulation data, disagree significantly with the analytically calculated values.

The data shown in Figure 11 seem to indicate that the largest benefit of strong injection-locking can be realized by operating the injection-locked laser along or near the Hopf bifurcation boundary as the largest bandwidth enhancement occurs there. However, this conclusion does not consider the noise of the laser. Figure 12 shows the total power of the amplitude noise of the laser under injection locking, normalized to that of the laser in the free-running condition, as a function of the injection parameter. Line *b* marks the noise level of the laser in the free-running condition. Again, each thick curve corresponds directly to the curves in Figures 10 and 11 that have the same label. Curves *d* and *e* cannot be distinguished in Figure 12 because they virtually overlap. Each of the thin dotted contour curves in Figure 12 shows how the total noise of the laser varies with the injection parameter when the frequency detuning of the injection signal is fixed at the value in gigahertz that labels a particular curve.

It can be seen that noise reduction by injection locking occurs only in the region between curves *b* and *e*. In the region above curve *b*, the laser noise increases dramatically as the operation condition approaches the Hopf bifurcation boundary marked by curve *a*. This is expected because dynamic instability of the injected laser starts to appear in the region above the Hopf bifurcation boundary. The significant effect of dynamic instability on the noise of the laser can be very clearly seen by following the contour line of zero frequency detuning. For injection at the free-running frequency of the laser with zero frequency detuning, the laser undergoes several different nonlinear dynamic states, including period doubling and chaos, when the injection parameter varies between $\xi = 0$ and $\xi \approx 0.18$. The high noise levels represented by the zero-detuning contour curve within this range are a clear indication of the instability associated with such nonlinear dynamics.

Though the region without noise reduction covers a large range between curves *a* and *b* in Figure 12, it represents only a small range of operation conditions shown in Figure 10 and a still

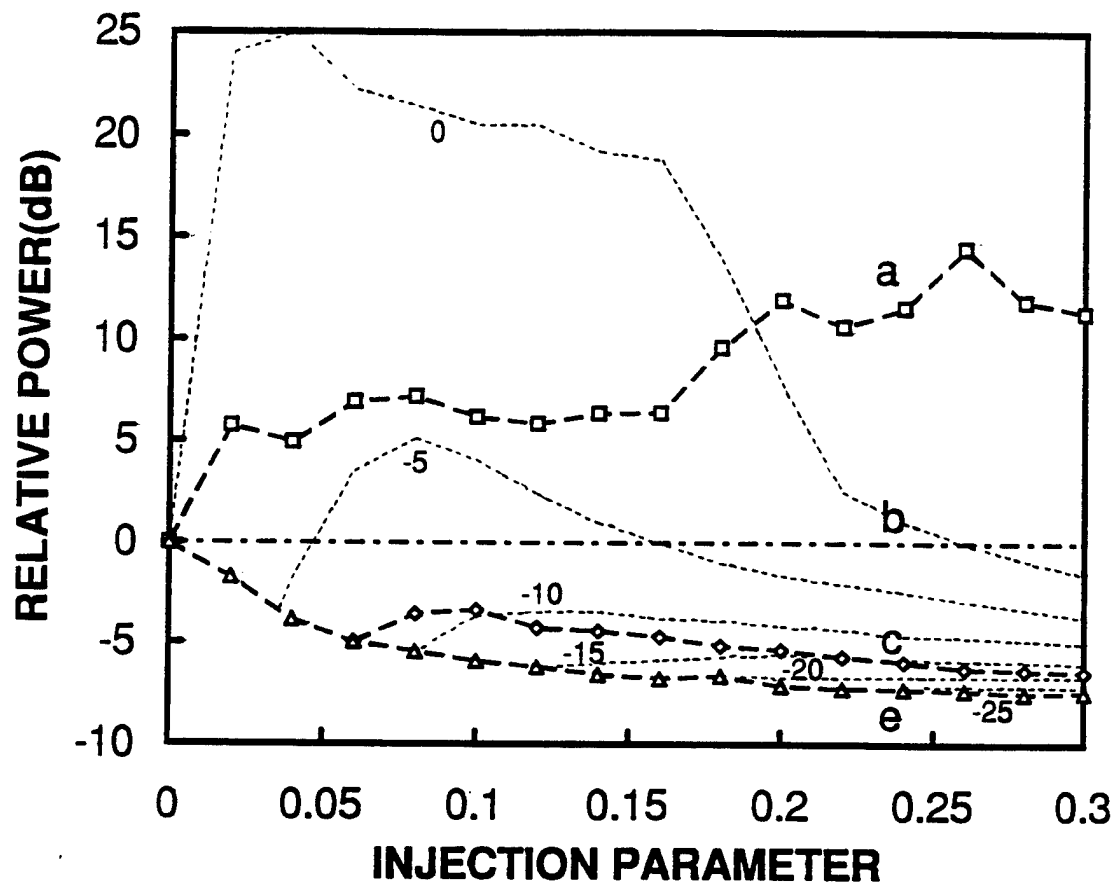


Figure 12: Total noise power of the laser under injection locking, normalized to that of the laser in the free-running condition, as a function of the injection parameter. Line *b* marks the noise level of the laser in the free-running condition. Each thick curve corresponds directly to the curves in Figures 10 and 11 that have the same label. Curves *d* and *e* cannot be distinguished in this figure because they virtually overlap. The thin dotted curves are contour curves for fixed values of frequency detuning in gigahertz.

smaller range of variation in the resonance frequency shown in Figure 11. In contrast, the bistability region bounded by curves *c* and *e* occupies a relatively large range of operation conditions shown in Figure 10 and an even larger range of variation in the resonance frequency shown in Figure 11, but it covers only a small range of maximum noise reduction shown in Figure 12. In the large region bounded by curves *b* and *c*, bandwidth enhancement, noise reduction, and stable locking can be simultaneously fulfilled.

By correlating the data shown in Figures 11 and 12, we find that when the injection parameter is fixed at a certain value, the frequency detuning for maximum bandwidth enhancement differs from that for maximum noise reduction. However, at a given value of frequency detuning, both bandwidth enhancement and noise reduction are improved as the injection parameter is increased over the range of parameters considered. At injection levels above those considered here, the resonance frequency can be sufficiently enhanced that there is a significant dip in the modulation response at frequencies below the resonance frequency [2]. Significant bandwidth enhancement coupled with noise reduction under a stable locking condition can be realized with a strong injection signal over a properly chosen frequency detuning range. For the laser biased at $\tilde{J} = 2/3$ that is considered in this paper, stable locking of the laser with an injection signal of $\xi = 0.3$ at a frequency detuning of -10 GHz triples the resonance frequency to 9 GHz while simultaneously reducing the total laser noise by 5 dB. Although the data discussed in this paper specifically apply to one laser, the qualitative conclusions obtained from this study apply to other semiconductor lasers in general.

4.3 VCSEL Characteristics

The effects of optical injection on the optical spectrum of a VCSEL are shown in Figure 13. For these spectra, the VCSEL was operated at a bias current of 6 mA. Again, zero frequency corresponds to the free-running optical frequency of the VCSEL. The master laser was also tuned to this frequency for this series of spectra. At this injection current level, there is some output power in higher order spatial modes which are spectrally offset from the region shown. Optical injection at the free-running frequency of the dominant, lowest order spatial mode, the case shown here, leads to a decrease in the power in the higher order modes. However, it did not fully quench this emission. The set of spectra in Figure 13 show an initially free-running laser, 13(a), which undergoes a Hopf bifurcation to a dynamically unstable state as the injection level is increased, 13(b). The resonance frequency monotonically increases as the injection level increases, 13(c)-13(e). Finally, the laser reestablishes stable dynamics at very high injection levels, 13(f). The progression is similar to the one previously observed. The laser did not show period doubling and a transition to chaotic dynamics because the linewidth enhancement factor had a relatively low value, $b = 2-3$. Earlier data taken when the laser displayed a larger linewidth enhancement factor clearly displayed the transition to chaos. All of these features are consistent with the dynamics expected from the coupled equation model.

The increase in the resonance frequency as a function of the injection level is shown in Figure 14. Here, the resonance frequency again shows the nearly linear dependence with the injection parameter seen in the earlier data on the conventional, edge-emitting laser. We have previously shown that this dependence falls off to a $2/3$ rds power, cube root of the injected

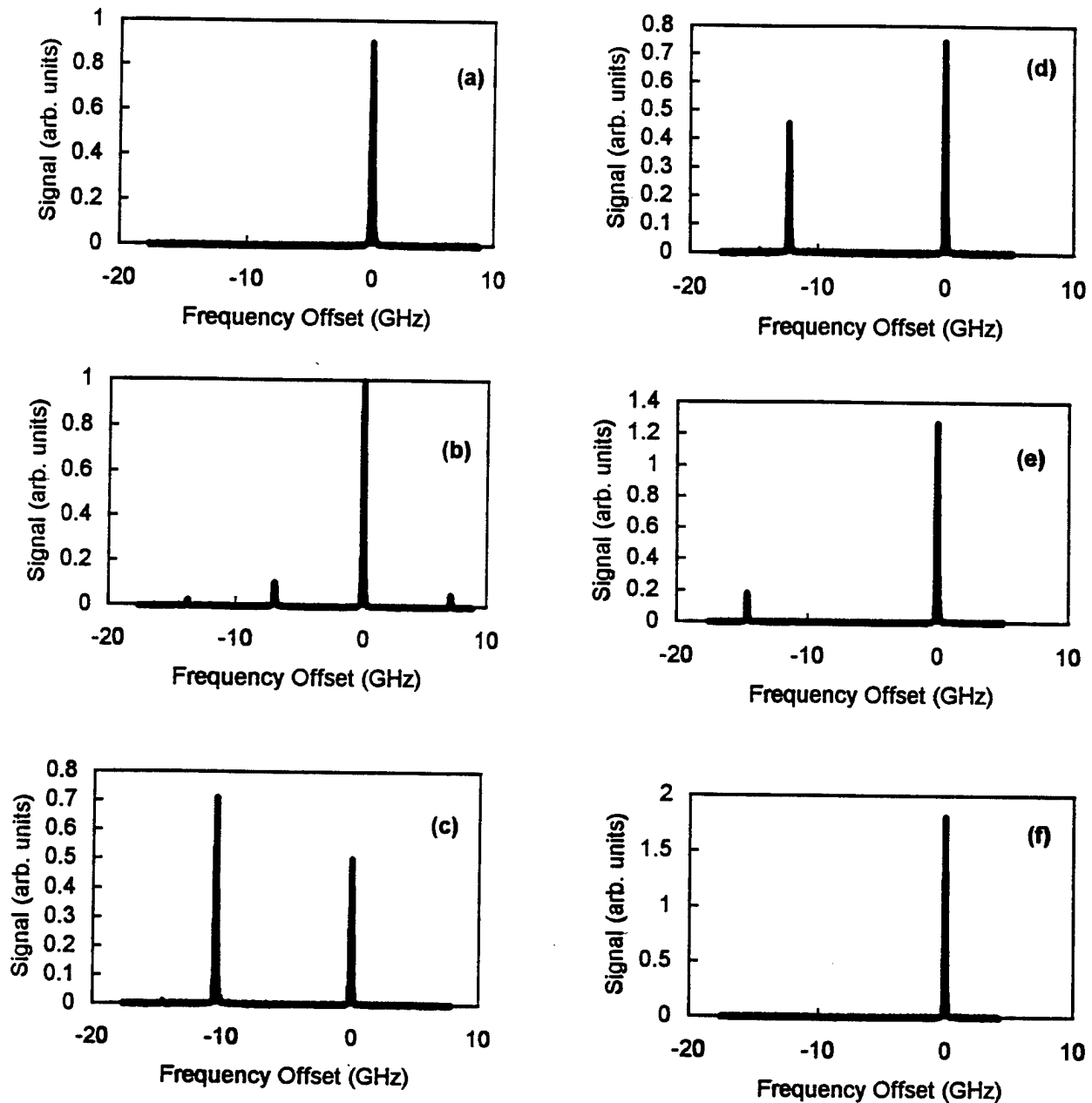


Figure 13: Measured optical spectra of the VCSEL with $\tilde{J} = 0.9$ under optical injection at the free-running frequency. The frequency axis is referenced to the free-running frequency of the VCSEL. The injection conditions are: (a) free-running and relative injection power levels of, in arbitrary units (b) 0.045, (c) 0.234, (d) 0.441, (e) 0.907, and (f) 1.536 where the laser has reestablished stable operation.

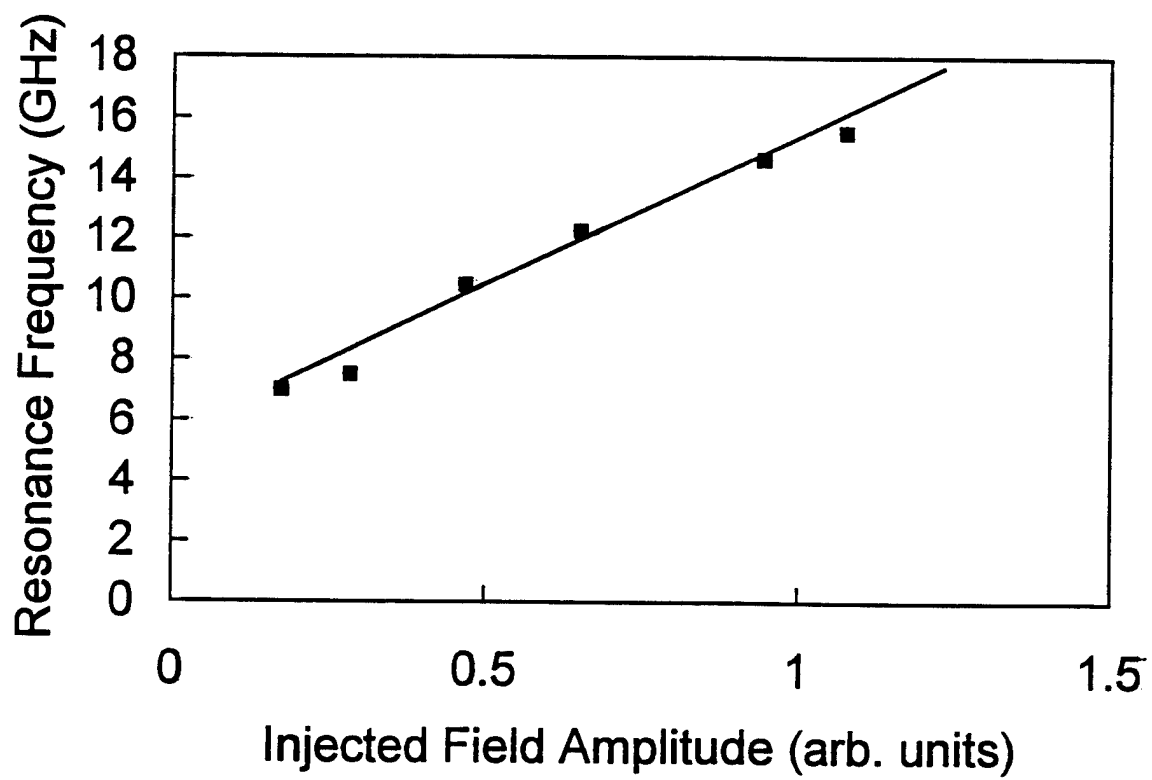


Figure 14: Variation of the resonance frequency of the VCSEL under external optical injection as a function of the square root of the injection power. The squares are the experimental data and the solid line is a visual aid.

power, when the injected power becomes large compared to the free-running output power [11]. Both of these results follow from the coupled equation model [2]. The spectra in Figures 13(c)-(e) show that there are two dominant components of the optical spectrum as the resonance frequency varies over a significant range of microwave frequencies. The beating of these two optical components leads to a strong microwave signal upon conventional detection of the optical beam. This tunability is achieved by changing the injected power from a cw optical beam without the requirement for any high-speed electrical input. The tuning range shown in Figure 14 should not be taken as a performance limit for VCSELs in general or even the VCSEL under study. Others have observed the changing resonance frequency in VCSELs to be as large as 60 GHz [21].

Referring back to the mapping of the conventional, edge-emitting laser, 8, some features of the mapping reflect specific characteristics of the laser under investigation, a conventional, edge-emitting, Fabry-Perot laser diode, where the oscillating mode is always in competition with other longitudinal modes which are close to threshold. Because of this, the external optical signal can induce a mode hop and certain regions of the detuning-injection plane become inaccessible. There is an abrupt mode hop near the locking-unlocking boundary which has a small hysteresis, not shown, associated with it. For larger offsets, some of the mode hops are one way and the laser does not reestablish operation on the original longitudinal mode at this boundary. At negative offsets there is a bounded range of unstable dynamics which follows a period-doubling progression, largely obscured by noise, to chaotic dynamics. Within the range of chaotic dynamics a varying fraction of the optical output begins to shift to other modes. One edge of the region of chaotic dynamics is an abrupt transition where power returns to the original longitudinal mode as the laser returns to oscillatory dynamics. Again there is a small hysteresis, not shown, associated with this transition.

Because the longitudinal modes in a VCSEL have such a large frequency spacing, only one is resonant with the high-reflectivity mirrors that define the laser cavity. Therefore, the VCSEL should not show these mode hops and we did not observe them. In addition, it should be able to show the locking/unlocking bistability that was apparently masked in the other laser by the mode hop. The bistability could be observed. Figure 15 shows a set of spectra taken with the bias current to the VCSEL set at 6 mA and the detuning of the master laser varied while the injection level was held constant. When the master laser frequency offset is shifted to negative values away from the free-running slave frequency, the laser remains locked until the detuning is beyond -12 GHz. However, when the detuning shift is then reversed, locking is not reestablished until -10.8 GHz. Between -12 and -10.8 GHz the laser displays the locking/unlocking bistability.

5. VCSEL NEAR THRESHOLD

The threshold for laser oscillation is a prototype for the disorder-to-order transition that occurs in a wide range of physical systems [22]. It has a strong analogy with phase transitions of systems in thermal equilibrium [23]. At such transition points, the fluctuations induced by noise sources play a critical role. Noise in lasers near threshold has been studied extensively, but most analyses have concentrated on laser systems where the refractive index of the gain medium is relatively unaffected by changes in the optical gain [24]. Here, we present data starting from a free-running

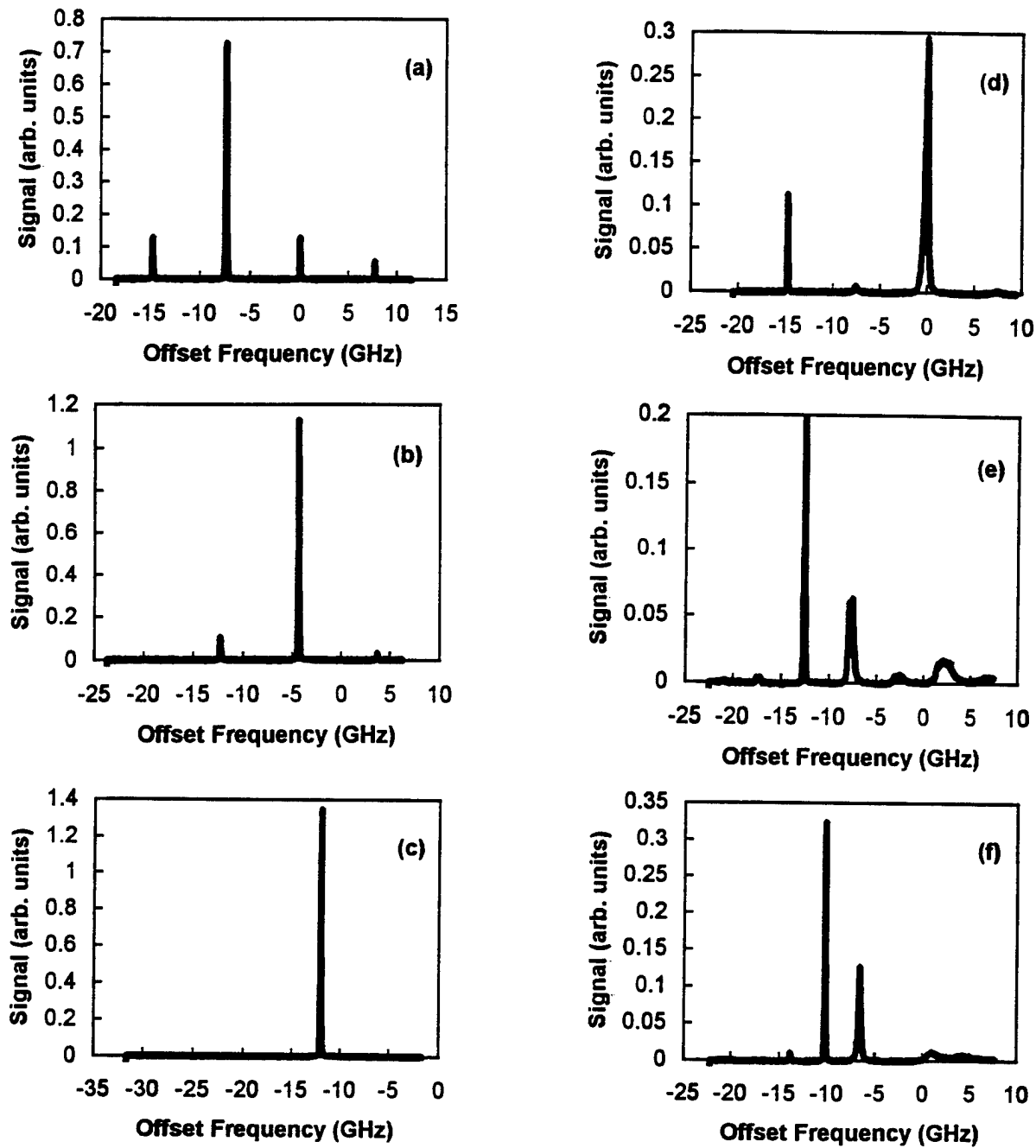


Figure 15: Measured optical spectra of the VCSEL with $\tilde{J} = 0.9$ as the injection frequency offset is shifted. The frequency axis is referenced to the free-running frequency of the VCSEL. Locked injection as the injection frequency is shifted away from resonance: (a) 0 GHz offset, (b) -4.8 GHz, (c) -12 GHz. Unlocked injection as the injection frequency is shifted towards resonance: (d) -15 GHz, (e) -12.6 GHz, and (f) -10.8 GHz.

condition which shows a striking change in the lineshape of the semiconductor laser. While the lineshape is Lorentzian below and well above the threshold region of laser oscillation, it is near Gaussian at and just above the threshold. The Gaussian lineshape reflects the fluctuations of the cavity resonance frequency due to the carrier density fluctuations. Injection of an external optical field induces spectral holes and spikes as well as an overall shift in the Gaussian lineshape. The typical optical spectra of a semiconductor laser undergoing deterministic chaos is observed as well as a transition back to linear dynamics and a Lorentzian lineshape of the field-noise-induced spectrum at high injection levels. We observed these features in a VCSEL. However, the key point is not that the laser structure is very different from the conventional edge-emitting laser described above. It is that this laser had significantly larger values of b and γ_c . The larger value of γ_c means that the laser is noisier. All novel features observed in the spectra could be recovered using the coupled equation model.

Well below and well above the threshold for laser oscillation, the lineshape of a semiconductor has been well studied and is well understood [8]. At an injection current of 3.8 mA, below the oscillation threshold, the laser exhibits a Lorentzian lineshape determined by the difference between the gain and γ_c , as shown in Figure 16(a). As has been observed previously, the linewidth of a semiconductor laser then begins to broaden as the injection current is increased [25] due to the linewidth-enhancing effects of b [8]. We also observe in the VCSEL, and this is a key experimental feature that we wish to emphasize here, that this broadening is accompanied by a change in the lineshape from Lorentzian to near Gaussian. This is shown in Figure 16(b) where the injection current to the VCSEL is 4.1 mA. As the injection current is increased further, the Lorentzian lineshape, accompanied by relaxation resonance sidebands, reappears. This is the typical optical spectrum of a semiconductor laser biased above threshold, and the spectrum for an injection current of 4.4 mA is shown in Figure 16(c). In the wings the laser lineshape falls off more rapidly than the Lorentzian curve. This feature, along with the relaxation resonances, has been previously observed in semiconductor lasers and explained by pointing out that the linewidth enhancement factor, acting through carrier density fluctuations, is not an instantaneous effect [8]. Ultimately, for large offset frequencies, a Lorentzian lineshape reflecting only field-noise sources acting directly on the optical phase should reappear. It has been previously established in lasers where changes in the gain are not accompanied by significant changes in the refractive index that the lineshape always remains Lorentzian [24]. Past work on the lineshape of semiconductor lasers near threshold has shown non-Lorentzian lineshapes, though this point has not been emphasized, but these lineshapes were not so clearly Gaussian as was observed in our laser [25].

We have calculated the optical spectra for the VCSEL using the coupled equation model. To emphasize the generic nature of the observed phenomena, we use a simplified form of the model. Near threshold, where the circulating optical field is small, it is more convenient to use as the reference point the injection current, J_0 , and the carrier density, N_0 , where $\Gamma g(N_0) = \gamma_c$ when no optical field is present. Coupled equations for the two quadrature components of the optical field then replace the equations for amplitude and phase used for the above-threshold case. Near threshold, we can ignore the contributions of γ_n and γ_p to the damping due to the small value of the field. We retain the important contributions of the field dependence to the cavity resonance frequency shift and to the field-carrier resonant coupling. If we make the assumptions that $\gamma_s = \gamma_n \tilde{J}$ when $\tilde{J} = 1$ and that cavity losses are due to output coupling only, then the coupled

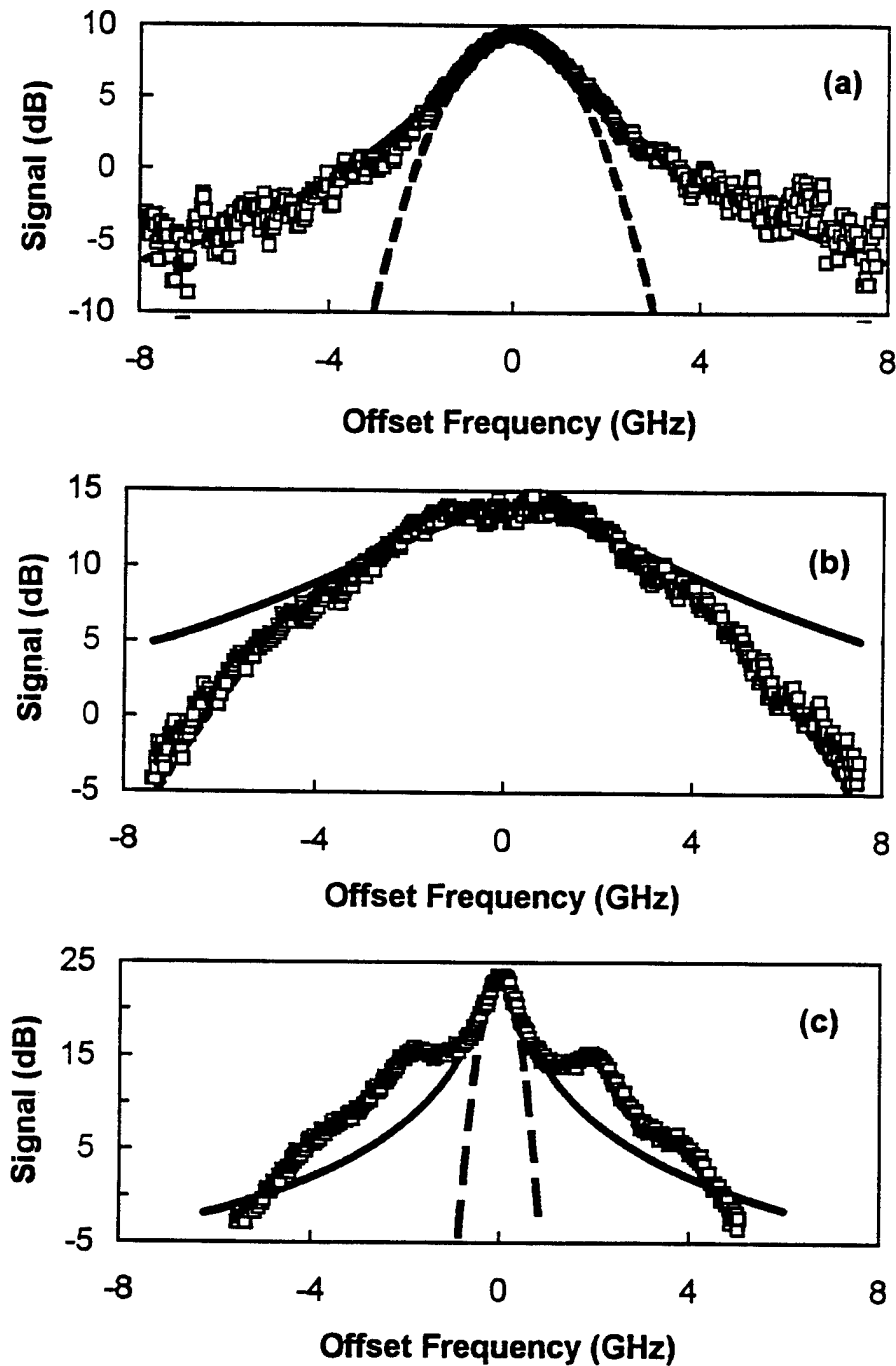


Figure 16: Measured optical spectra of a VCSEL as the bias current is varied: (a) 3.8 mA, just below the oscillation threshold, (b) 4.1 mA, above the oscillation threshold, and (c) 4.4 mA, approximately 10% above the oscillation threshold. Also shown are Lorentzian (solid line) and Gaussian (dashed line) curves fit to match the spectra full width at half maximum.

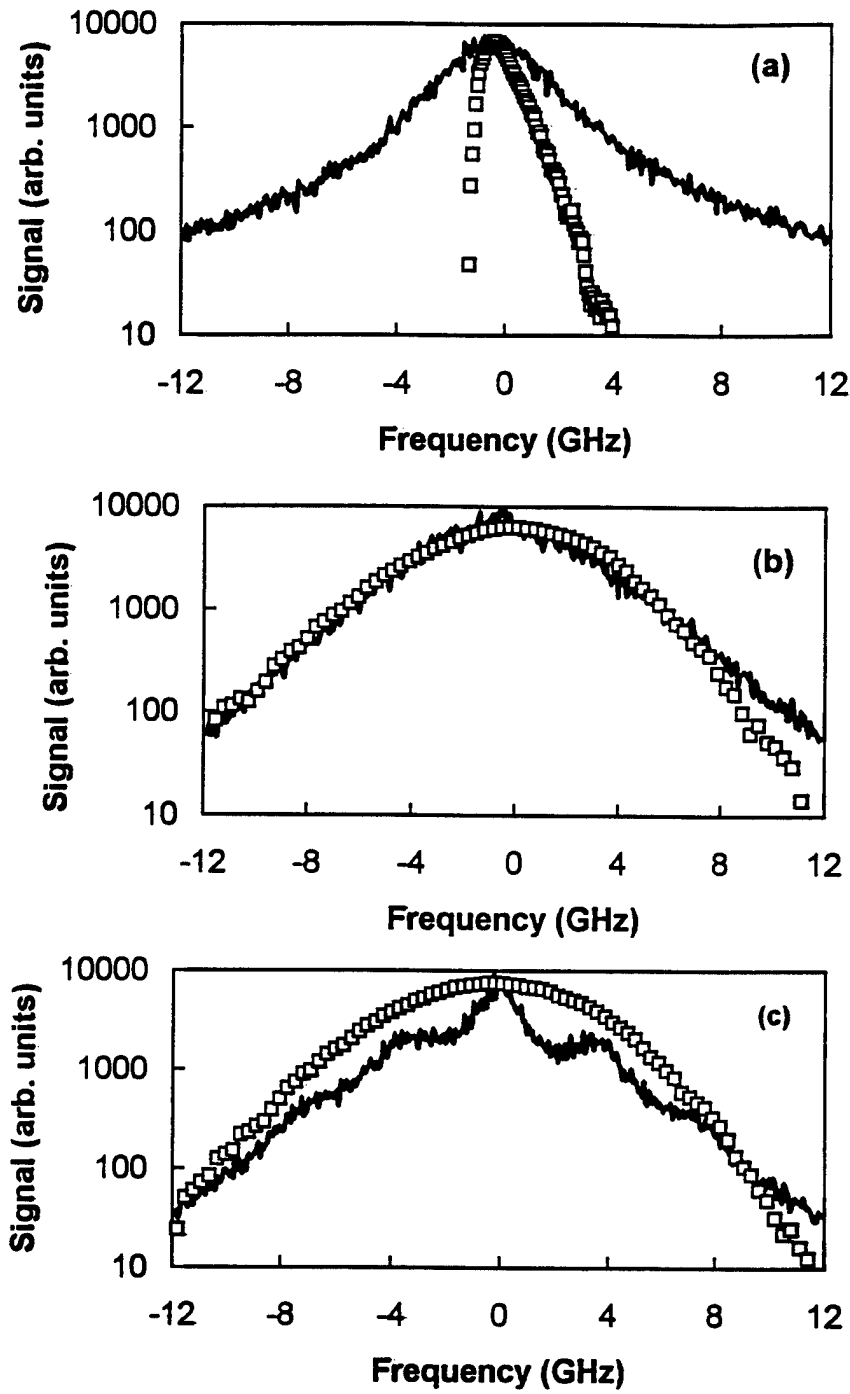


Figure 17: Calculated optical spectra (solid line) and histograms of the Fabry-Perot resonance frequency variation based on fluctuations in the carrier density (squares) using the experimentally determined VCSEL parameters for different values of the normalized bias current parameter: (a) $\Delta = -0.02$, (b) $\Delta = 0.1$, and (c) $\Delta = 0.2$.

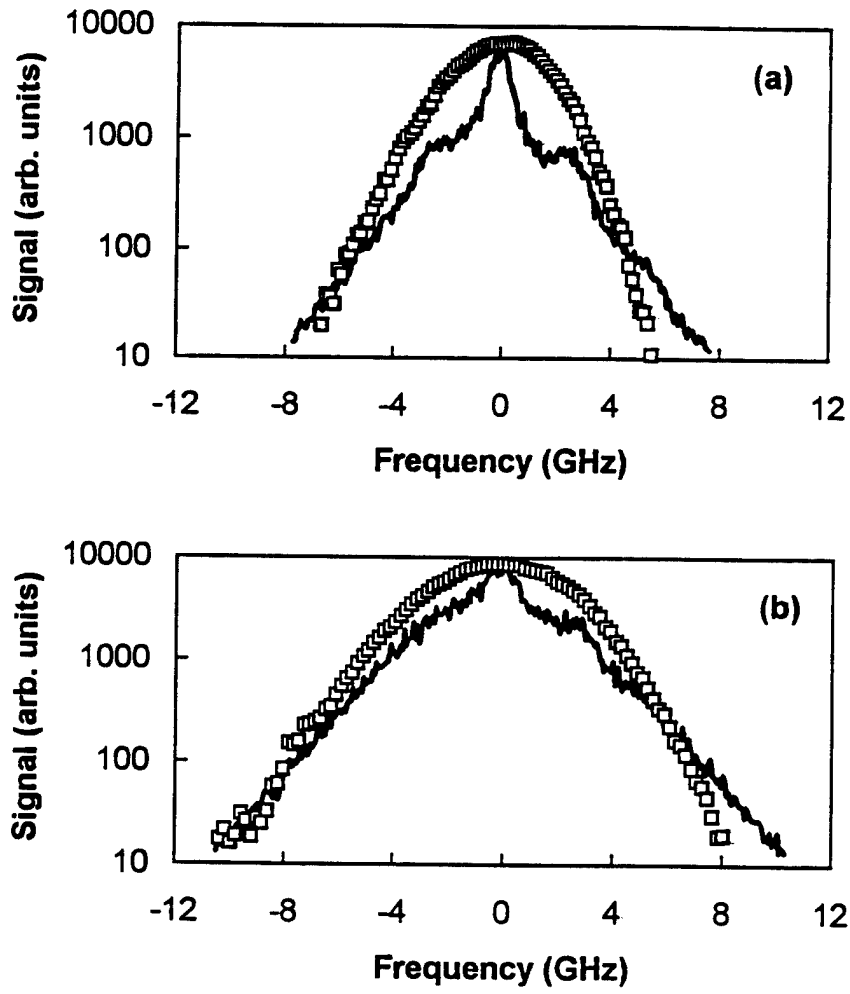


Figure 18: Calculated optical spectra (solid line) and histograms of the Fabry-Perot resonance frequency variation based on fluctuations in the carrier density (squares) using modified values of the the experimentally determined VCSEL parameters for the case of Figure 16(b). In (a) the linewidth enhancement factor, $b = 3$, not 6, and in (b) the field noise power is reduced by a factor of 2. All other parameters remain the same.

equations take on a particularly simple form.

$$\frac{dE_1}{dt} = \frac{\gamma_c}{2}(E_1 + bE_2)\tilde{n} + A_i \cos(\Omega t) + F_1, \quad (9)$$

$$\frac{dE_2}{dt} = -\frac{\gamma_c}{2}(bE_1 - E_2)\tilde{n} - A_i \sin(\Omega t) + F_2, \quad (10)$$

$$\frac{d\tilde{n}}{dt} = \gamma_s(\Delta - \tilde{n}) - \frac{2\epsilon_0 n^2}{\hbar\omega_0} g_N(E_1^2 + E_2^2). \quad (11)$$

Here, E_1 and E_2 and F_1 and F_2 are the quadrature field and field-noise components, respectively. The experimentally accessible control parameter is the injection current which is normalized for numerical calculation in the parameter $\Delta = (J - J_0)/ed/\gamma_s N_0$. A convenient normalization for the equations can be made by defining $R_{sp} = \gamma_c F_0^2$ and normalizing the field equations with respect to F_0 . Values for the parameters are derived from previously reported data [11] with $b = 6$, $\gamma_c = 5 \times 10^{11} \text{ s}^{-1}$, $\gamma_s = 1.1 \times 10^{-2} \gamma_c$, and

$$\frac{2\epsilon_0 n^2}{\hbar\omega_0} g_N F_0^2 = 10^{-6} \gamma_c. \quad (12)$$

Using the simplified equations, we can recover the transition from Lorentzian to near Gaussian to Lorentzian as Δ , or the injection current, is increased. Calculated optical spectra of the free-running laser are plotted in Figure 17. Due to the more simplified model, the agreement is relatively less quantitative than for the edge-emitting laser described above. Lorentzian wings are calculated for the near-Gaussian lineshape at offset frequencies beyond 25 GHz. If, however, the linewidth enhancement factor is reduced to $b = 3$, or the strength of the noise power, R_{sp} , is reduced by a factor of 2, the Gaussian lineshape at $\Delta = 0.1$ disappears, as shown in Figure 18. In either of these cases the lineshape remains essentially Lorentzian, with the relaxation resonance sidebands above threshold, throughout. We should point out that a change in the noise power is also equivalent to a simultaneous scaling of γ_s and g_N because of the intimate relationship between R_{sp} and γ_c [26].

Unlike the optical spectrum, the amplitude (intensity) spectrum of the laser field and the spectrum of carrier density fluctuations are not influenced by a change in the linewidth enhancement factor. Similarly, for the range of values considered here, they show only minor changes in shape, accompanied by an overall scaling in strength, due to a change in the amplitude of the noise source. The calculated spectra for the intensity and carrier density follow the expected profile from a linearized analysis [5], except at low frequencies due to the incomplete amplitude pinning near threshold. The amplitude of the laser field and the carrier density are mutually coupled but are independent of the phase of the field. While the phase fluctuations do not couple back to these two quantities, they are strongly influenced by them through the linewidth enhancement factor and the dependence of the gain on the carrier density. However, the near-Gaussian lineshape is not a result of nonlinear dynamics. All three equations can be linearized and the same lineshape will appear. In a semiconductor laser, the Lorentzian lineshape occurs when the relaxation resonances are well outside of the central linewidth so that the resonant peaks separated by the relaxation resonance frequency overlap weakly [8, 27]. Near threshold this approximation will fail. In cavities characterized by a fast photon decay rate, with correspondingly large field-noise source term, and a large linewidth enhancement factor, like the VCSEL studied here, strong deviations from the Lorentzian lineshape can be expected.

To determine the source of the near-Gaussian lineshape it is necessary to analyze the calculated time series for the carrier density equation. The carrier density fluctuations are proportional to index of refraction changes through the dependence of the gain on the carrier density. These fluctuations lead to instantaneous variations in the cavity resonant frequency. A histogram of the frequency variations is also shown in Figures 17(a) and 18. It is generated by counting the number of times the frequency (carrier density) value falls within a frequency bin interval and plotting the count as a function of frequency. This generates a curve with values proportional to the fraction of time that the particular frequency bin is the instantaneous resonant frequency. The curve of resonant frequencies is dissimilar to the laser lineshape in Figures 17(a) and (c) and in Figure 18, but follows the same Gaussian profile in Figure 17(b). At this pump level, it is the range of carrier density fluctuations that determine the laser lineshape and not the usual phase diffusion fluctuations. The instantaneous cavity resonant frequency fluctuations are caused by the same field-noise source terms as the phase diffusion fluctuations, but usually they are not a significant factor in determining the lineshape because the linewidth of each of the relaxation resonance features that forms the overall lineshape is less than the resonance frequency. Therefore, the normal phase diffusion term reasserts its dominance above threshold even though the carrier density fluctuations persist. Only when the different relaxation resonance components show substantial overlap is there strong deviation from a central Lorentzian lineshape.

When the free-running Gaussian-lineshape laser is subjected to external optical injection, several spectral changes occur. As before, we first concentrate on resonant injection. The first observable change as the injection level is increased is a shifting of the spectrum to lower optical frequencies. This reflects the drop in the overall carrier density due to the higher circulating field and enhanced stimulated emission. As the injection level is increased further, the spectrum shows a new spike at negative offset frequencies and a dip at positive offset frequencies in addition to the overall shift and a spike at the injection frequency, as shown in Figure 19(a). The free-running spectrum is also shown for reference. The spike and dip are oppositely offset by 1 GHz, approximately the relaxation resonance frequency. As the excitation level is increased further, spikes and dips appear at multiples of the original offset, corresponding to the different resonance features. At higher excitation levels, the spectra are similar to the chaotic dynamics spectra discussed above, Figure 19(b). Finally, at very high excitation levels, the spectral structure has shifted away from the excitation peak and assumed a more Lorentzian lineshape, Figure 16(c). Calculated spectra show the progression from shift with spike and dip, Figure 20(a), to chaotic-like, Figure 20(b), to shifted Lorentzian, Figure 20(c).

We have previously presented the shift of the Fabry-Perot resonance feature due to optical injection when this laser was initially biased at 3.9 mA, at the laser threshold [11]. There, the initial deviation from Lorentzian was not large but the spectra clearly showed a narrowing and a progression to a more Lorentzian lineshape as the injected power was increased. This effect can also be seen as the laser frequency is tuned across the resonance at strong injection levels at the higher operating current described by the spectra presented here. Figure 21 plots this trend under strong external injection. For large positive detunings the Gaussian lineshape is retained but there is a shift of the feature. As the detuning is decreased the feature narrows, with increased amplitude. For injection close to the edge of the locking range, near -24 GHz, the emission feature becomes weak, indicating stable, injection-locked operation. The smooth progression of the shift of the Fabry-Perot resonance feature is summarized in Figure 22. For positive detunings, the

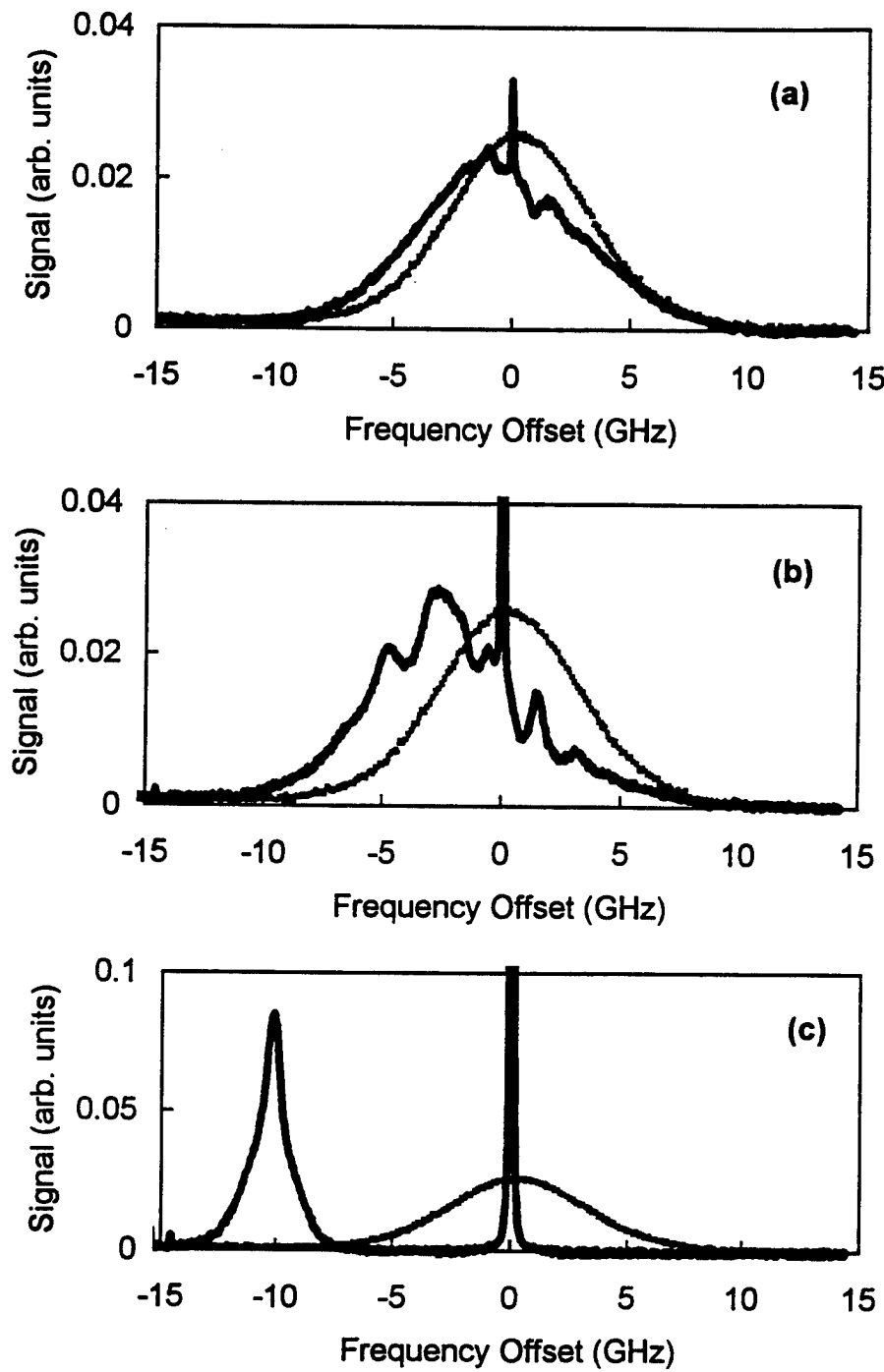


Figure 19: Measured optical spectra of the VCSEL biased at 4.1 mA and subjected to external optical injection. The ratio of injected power is: (a) 1, (b) 10, (c) 940. The free-running spectrum is also shown for reference.

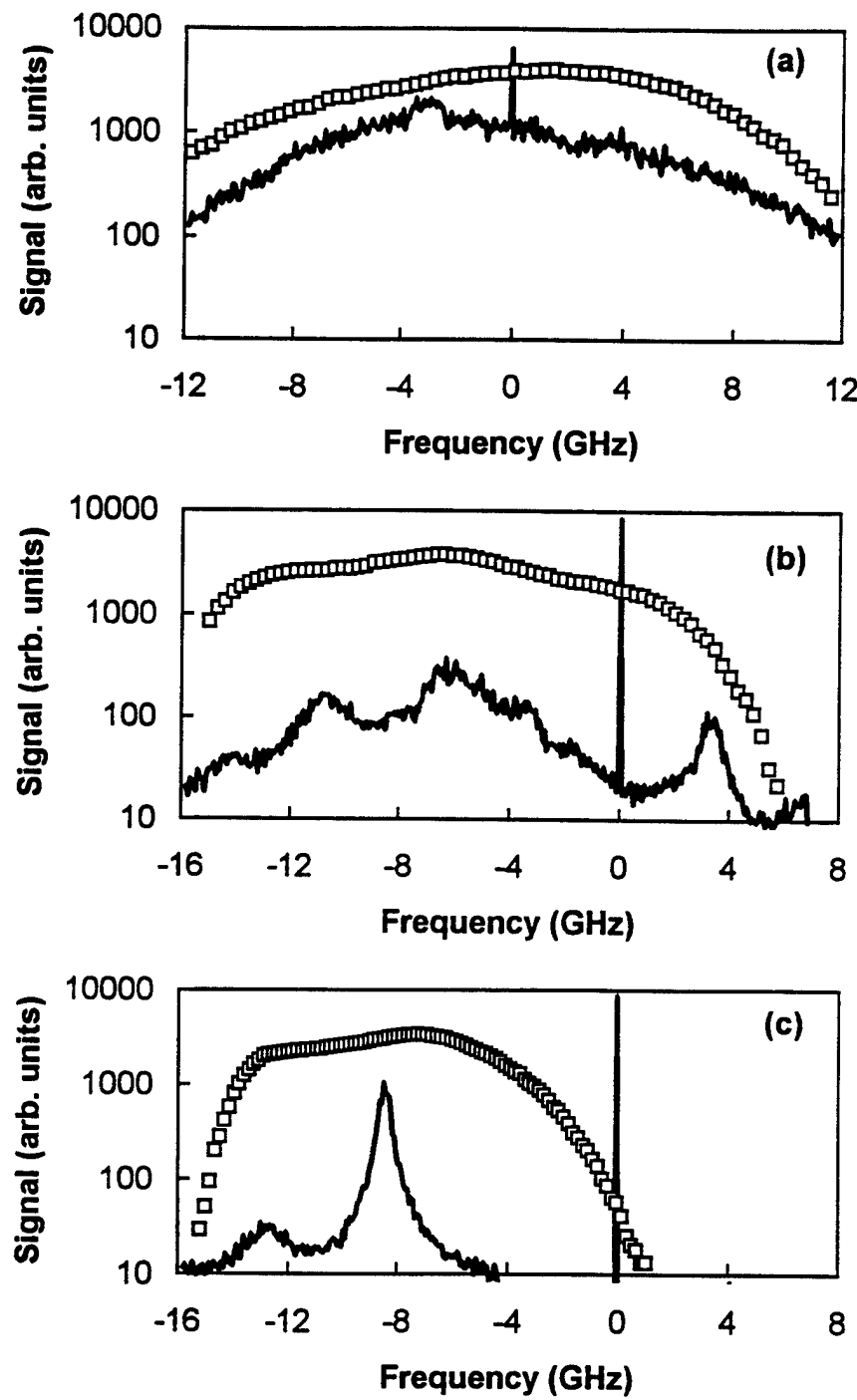


Figure 20: Calculated optical spectra of the VCSEL biased at 4.1 mA and subjected to external optical injection. The ratio of injected optical power is: (a) 1, (b) 4, (c) 100.

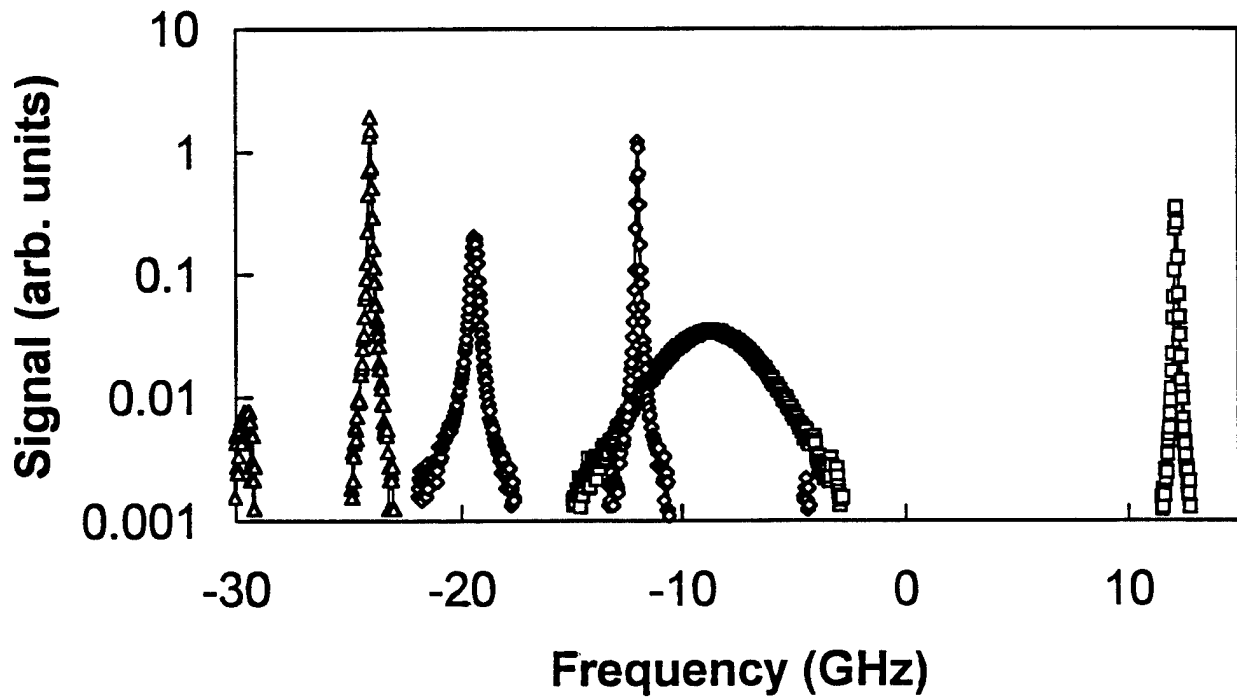


Figure 21: Spectra of the VCSEL under strong optical injection as the detuning is varied: 12 GHz (squares), -12 GHz (diamonds), and -24 GHz (triangles). Each spectrum has two principal features, the regeneratively amplified injected signal and the regeneratively amplified spontaneous emission at the shifted Fabry-Perot resonance peak of -8.5 GHz, -19.5 GHz, and -29.5 GHz, respectively. The -12 GHz offset excitation spectrum also shows a weak four-wave mixing peak at -4.5 GHz.

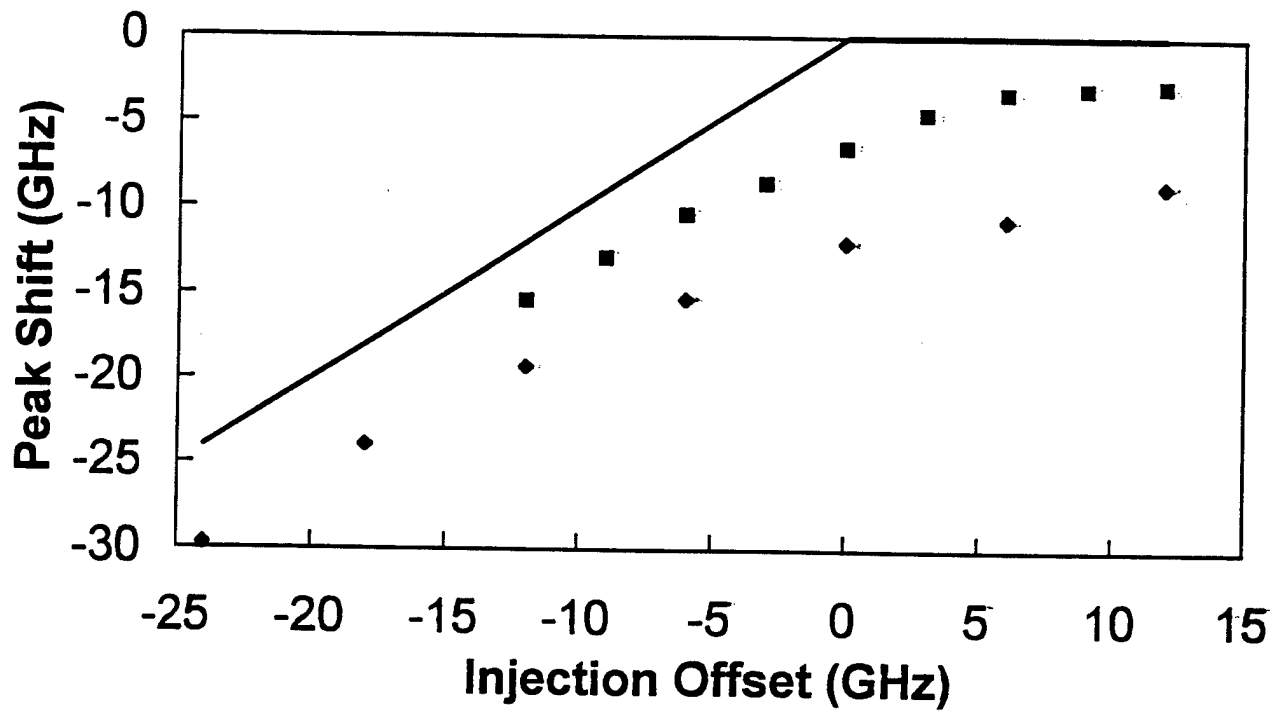


Figure 22: Measured pushing of the Fabry-Perot resonance as a function of the detuning of the injected signal. The diamonds are for an injected power approximately an order of magnitude stronger than the squares. The solid line is a slope of one line at negative offsets and slope of zero line at positive offsets to aid the eye.

shift decreases with increasing offset as the injection undergoes less amplification in the cavity. For negative detunings the shift is greater than but approaching the magnitude of the injection offset as the offset decreases to more negative values. At the edge of the locking range this smooth progression abruptly halts and the laser displays a weaker, more complex spectrum. The shift of the cavity resonance frequency and the associated damping are caused by the reduced carrier density under strong external injection. The dynamics are strongly influenced by the magnitude of the shift and damping.

6. VCSEL POLARIZATION AND NOISE CHARACTERISTICS

The fact that the VCSEL has two nearly degenerate, orthogonally polarized modes can complicate the interpretation of the laser spectra. Even when the output power of one polarization dominates the other by a factor of 100, the influence of the weak polarization component is easily observed. First, it causes a broadening of the laser linewidth by more than a factor of 10. Second, it causes a resonance feature in the amplitude (power) spectrum. Figure 23 shows a key characteristic of this resonance. In the figure the reference is centered at approximately 600 MHz, 0 dB corresponds to the noise level of the measurement apparatus and -5 dB is the resolution limit. Three different power spectra are shown. When the measured polarization component is directed to be along either of the two orthogonally polarized components, the resonance feature is at a relative maximum. However, when the measured polarization direction is rotated to be 45 degrees between the two polarization components, equivalent to measuring the total spectrum without polarization selection, the resonance feature essentially disappears. This shows that the two polarization components display anti-correlated dynamics. Power in one component comes explicitly at the expense of the other so that the total power is left unchanged.

External optical injection into either of the two components can cause an enhancement or a quenching of the resonance depending on the specific injection frequency and power. This is similar to the previously discussed case where the optical injection can cause unstable dynamics or stable injection locking in the single polarization case. Optical spectra under optical injection are shown in Figure 24. Here, the laser was operated at $\tilde{J} = 0.31$, zero frequency corresponds to the free-running frequency of the dominant peak and the orthogonal polarization component is offset by approximately 8.5 GHz. In both cases, injection on the strong peak, Figure 24(a), and the weak peak, Figure 24(b), the injection matches the polarization direction of the injected component. In the weak component spectra, there is residual signal from the strong component passed by our polarizers. In this spectra, therefore, we see the effect of the injection on the stronger orthogonal component. The orthogonal component shows resonance sidebands due to the injection. Little effect was observed when the polarization of the injected signal was orthogonal to the injected component. The injection strength was not sufficient to induce unstable dynamics directly in the strong component at the offset of the weak component. While the central peak of both polarization components is narrowed by the injection, indicating a quenching of the resonance, the dominant polarization component is clearly destabilized. Even more complicated spectra due to optical injection are observed when the two polarization components are of nearly equal strength in the free-running case. Figure 25 shows the case when $\tilde{J} = 0.38$

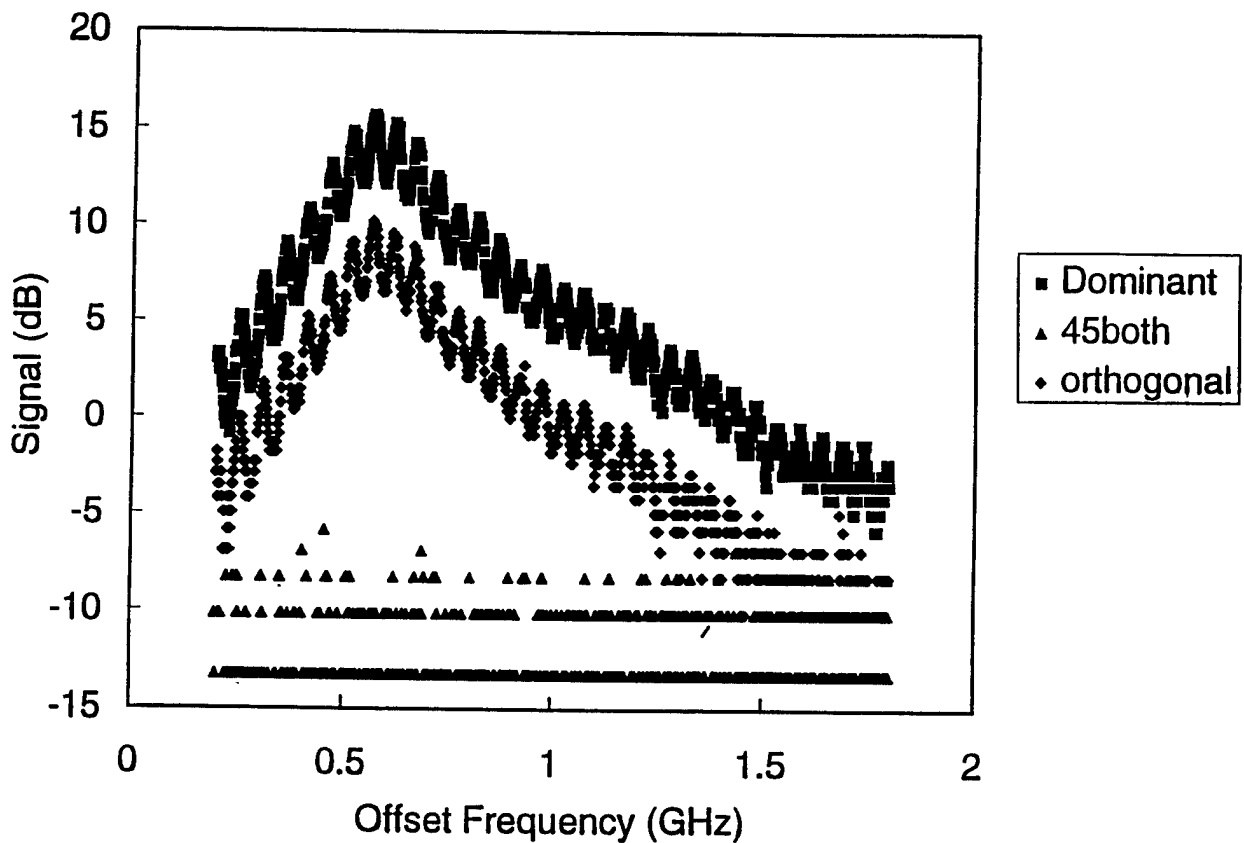


Figure 23: Low-frequency power spectrum showing the resonance due to the antimode coupling between the two orthogonally polarized modes. The VCSEL was operated at $\tilde{J} = 0.31$ where the dominant polarization is approximately two orders of magnitude stronger than the orthogonal component. The resonance disappears when the output polarized 45 degrees between the two orthogonal polarizations is passed to the photodetector.

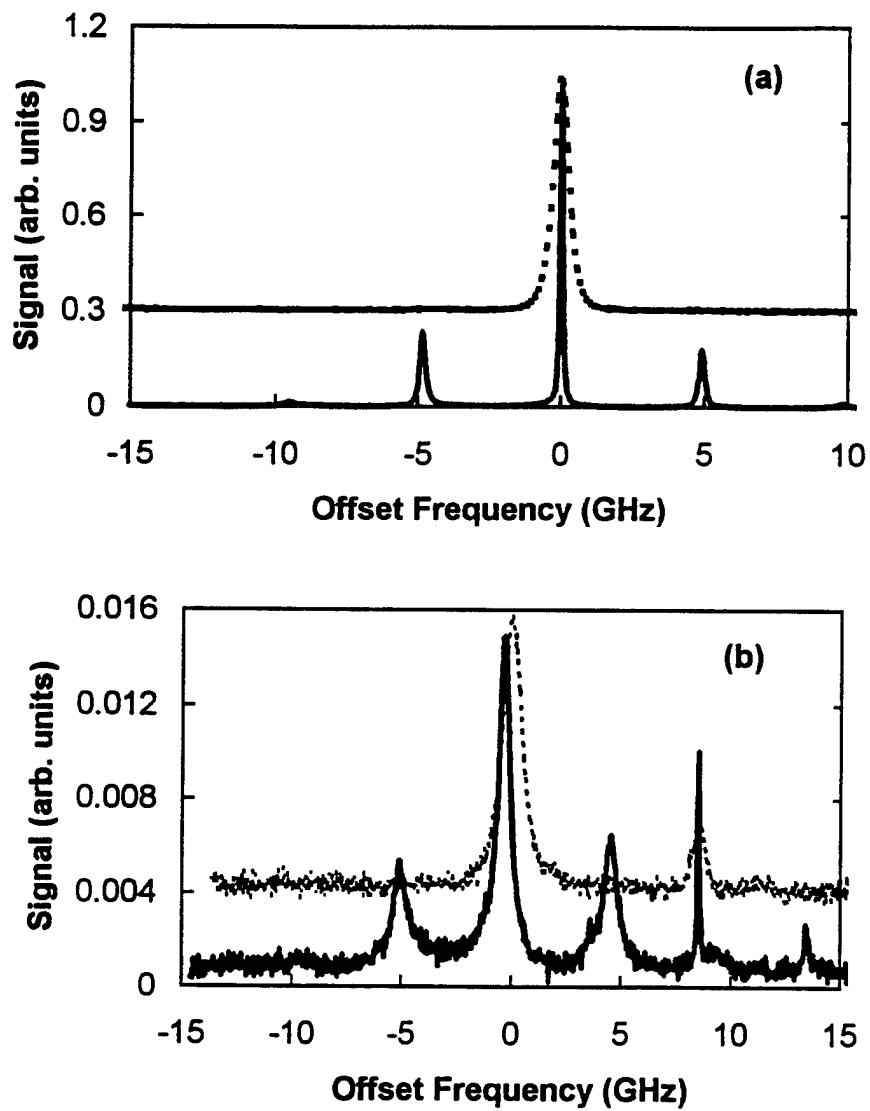


Figure 24: Optical spectra showing the effect of external optical injection on the two polarization components. $\tilde{J} = 0.31$, (a) injection and measurement parallel to the strong polarization component, and (b) injection and measurement parallel to the weak polarization component. The free-running spectra are shown offset for clarity.

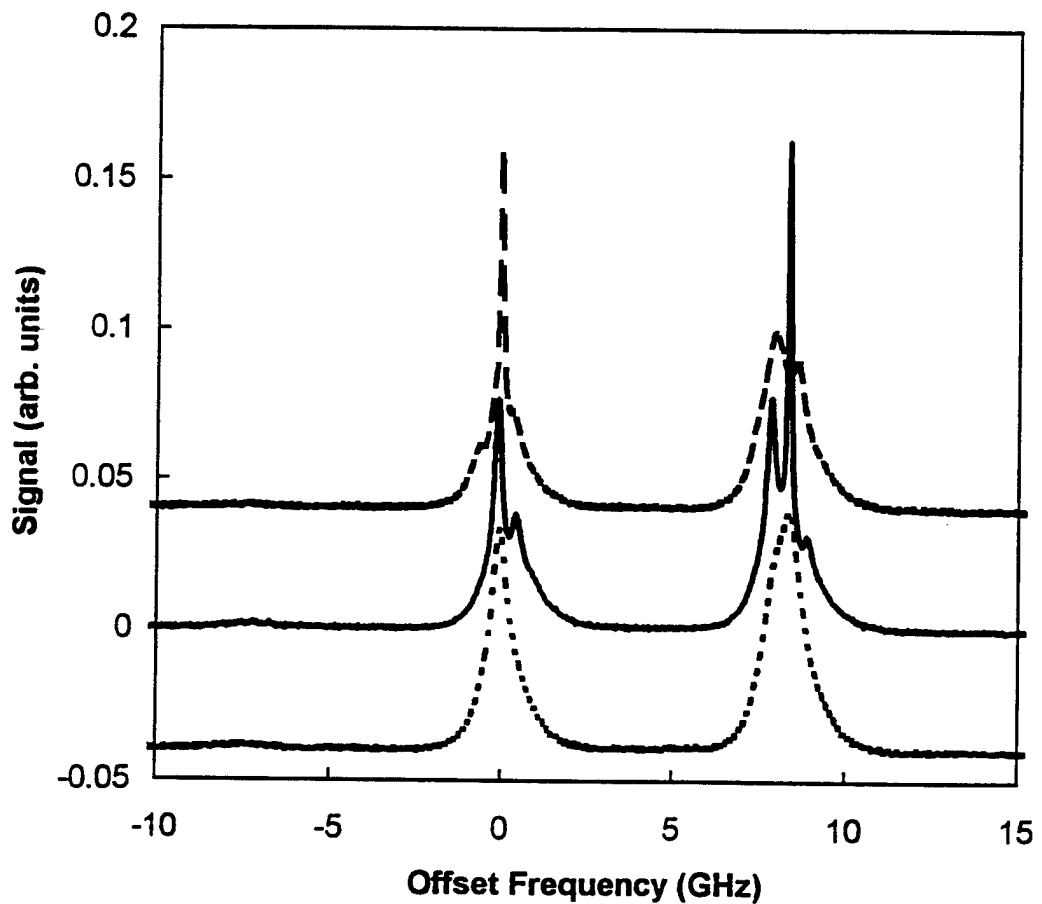


Figure 25: Optical spectra showing the effects of optical injection when the two polarization components are of similar magnitude, $\tilde{J} = 0.38$. Top, injection on the left peak. Middle, injection on the right peak. Bottom, free-running. The spectra are offset for clarity.

and the measured polarization direction is 45 degrees between the two polarization components. Injection on either peak induces a complicated structure. The details of this structure are not well understood. However, they clearly represent additional noise-like background in any modulation spectrum. For this reason, it is necessary to avoid VCSEL operation when there are two polarization components present for the types of applications that we have proposed in this program.

A more general problem was the strong influence of the intrinsic spontaneous emission noise on the spectral features. Proposed applications of rfmm systems require low noise signals of good spectral purity. However, when the laser was operated under conditions where there would be a strong microwave modulation frequency, the resonance feature was quite broad. Figure 26 shows a typical example. The master laser, and thus the optical component at the locking frequency, had an linewidth of under 5 MHz. Therefore, the shifted Fabry-Perot resonance component was not locked but had a much broader linewidth, yielding the order of magnitude larger linewidth of the microwave modulation component in the power spectrum. The spontaneous emission noise broadens the shifted resonance feature and breaks the locking of the master laser. We have calculated the effects of a current modulation at the resonance frequency, in addition to the injected optical signal. The modulation current has the effect of locking the two optical components together and sharply reducing the linewidth. However, the modulation component continued to retain fairly strong noise sidebands. Clearly, the noise characteristics of the VCSEL under investigation are not acceptable for the types of analog rfmm systems requiring good spectral purity.

Due to the effects of the polarization instability and the excitation of higher order transverse modes at higher bias currents, the VCSEL under investigation had a relatively narrow range of operating conditions where it had the potential to operate as a single-mode device. Single-mode semiconductor laser noise characteristics generally can be improved significantly by pushing the bias current far above threshold. However, the ability to do this with the VCSEL was limited by the appearance of the higher order transverse modes. This problem is not intrinsic to VCSELs and better devices are being reported in the literature.

7. CONCLUSIONS AND ACKNOWLEDGMENTS

The work done under this Phase I SBIR program has confirmed that the coupled equation model for a semiconductor laser under optical injection describes all of the key phenomena that we observe through the spectral characteristics. We have been able to generate a broadly tunable modulation signal when the master laser is tuned to generate an appropriate condition of unstable dynamics. Further, several novel spectral characteristics of the VCSEL, including a Gaussian lineshape near threshold, strong frequency pushing of the Fabry-Perot resonance signal, and a locking/unlocking bistability have all been understood by comparing measured spectra with the predictions of the model. However, the microwave signal generated by the beating of optical components is quite noisy when the laser is excited to display unstable dynamics due to the strong effects of spontaneous emission noise. Further work is necessary to improve VCSEL characteristics and to implement noise reduction techniques for the VCSEL to be useful in analog rfmm applications.

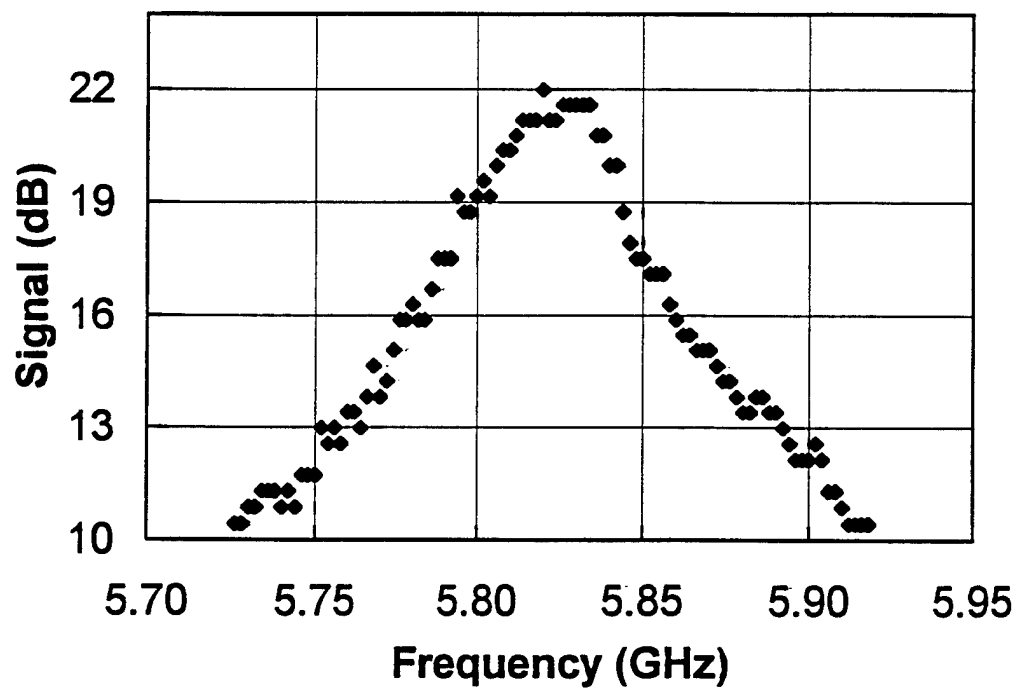


Figure 26: Power spectrum at the beat frequency between the injection-locked optical signal component and the shifted Fabry-Perot cavity resonance feature for the laser under optical injection where the optical spectrum showed two strong optical components. The bias current was 4.8 mA and the master laser had a linewidth of under 5 MHz.

Because VCSEL technology, especially with respect to single-spatial mode, single polarization devices, is still in the development phase, we recommend that further research on the application of injection-locked semiconductor laser technology to rfmm systems be broadened to include several more conventional devices. These can be chosen to answer specific questions which are directly related to findings of our Phase I research. First, because the ultimate interest is in devices which can be modulated at millimeter-wave frequencies, it is necessary to work with high-speed modulation devices. At the present time, conventional Fabry-Perot or distributed feedback laser diodes operating in the 1300-nm region are commercially available. Reports of modulation bandwidths of VCSELs above 20 GHz are in the literature but the conventional devices are reported to have modulation bandwidths above 30 GHz. Second, the more conventional devices can be operated farther above threshold and have better noise characteristics. This will allow follow-on research to separate the intrinsic semiconductor laser noise issues from those in VCSELs that relate more to the state of device development. Under strong injection locking, semiconductor lasers are calculated to be able to achieve bandwidths broadly tunable in the millimeter-wave region, with tunable modulation characteristics and reduced noise relative to the free-running case. This technique may be very useful for augmenting the performance of available laser diodes so that they can be useful in a variety of rfmm applications.

Some of the work described in this report was supported, in part, by the Air Force's Phillips Laboratory under contracts No. F29601-94-C-0166 and F29601-96-C-0047. The authors wish to thank Drs. C. Clayton, A. Gavrielides and V. Kovanis for helpful discussions.

References

- [1] T.B. Simpson, J.M. Liu, and A. Gavrielides, "Bandwidth enhancement and broadband noise reduction in injection-locked semiconductor lasers," *IEEE Photonics Technology Letters*, 7(7), 709–711, July 1995.
- [2] T.B. Simpson, J.M. Liu, and A. Gavrielides, "Small signal analysis of modulation characteristics in a semiconductor laser subject to strong optical injection," *IEEE Journal of Quantum Electronics*, 32(8), 1456–1468, August 1996.
- [3] J.R. Tredicce, F.T. Arecchi, G.L. Lippi, and G.P. Puccioni, "Instabilities in lasers with an injected signal," *Journal of Optical Society of America B*, 2(1), 173–183, January 1985.
- [4] J.M. Liu and T.B. Simpson, "Four-wave mixing and optical modulation in a semiconductor laser," *IEEE Journal of Quantum Electronics*, 30(4), 957–965, April 1994.
- [5] T.B. Simpson and J.M. Liu, "Spontaneous emission, nonlinear optical coupling and noise in laser diodes," *Optics Communications*, 112(1), 43–47, 1 November 1994.
- [6] T.B. Simpson, J.M. Liu, A. Gavrielides, V. Kovanis, and P.M. Alsing, "Period-doubling cascades and chaos in semiconductor lasers subject to optical injection," *Physical Review A*, 51(5), 4181–4185, May 1995.
- [7] Y. Yamamoto, S. Machida, and O. Nilsson, "Amplitude squeezing in a pump-noise-suppressed laser oscillator," *Physical Review A*, 34(5), 4025–4042, November 1986.
- [8] C.H. Henry, "Phase noise in semiconductor lasers," *IEEE Journal of Lightwave Technology*, LT-4(3), 298–311, March 1986.
- [9] H.M. Chen, K. Tai, K.F. Huamg, Y.H. Kao, and J.D. Wynn, "Instability in surface emitting lasers due to external feedback," *Journal of Applied Physics*, 73(1), 16–19, 1 January 1993.
- [10] K. Tai, Y. Lai, K.F. Huang, T.C. Huang, T.D. Lee, and C.C. Wu, "Transverse mode emission characteristics of gain-guided surface emitting lasers," *Applied Physics Letters*, 63(19), 2624–2646, 8 November 1994.
- [11] T.B. Simpson, J.M. Liu, K.F. Huang, K. Tai, C.M. Clayton, A. Gavrielides, and V. Kovanis, "Cavity enhancement of resonant frequencies in semiconductor lasers subject to optical injection," *Physical Review A*, 52(6), R4348–R4351, December 1995.
- [12] T.B. Simpson, J.M. Liu, A. Gavrielides, V. Kovanis, and P.M. Alsing, "Period-doubling route to chaos in a semiconductor laser subject to external optical injection," *Applied Physics Letters*, 64(26), 3539–3541, 27 June 1994.
- [13] I. Petitbon, P. Gallion, G. Debarge, and C. Chabran, "Locking bandwidth and relaxation oscillations of an injection-locked semiconductor laser," *IEEE Journal of Quantum Electronics*, 24(2), 148–154, February 1988.

- [14] V. Kovanis, A. Gavrielides, T.B. Simpson, and J.M. Liu, "Instabilities and chaos in optically injected semiconductor lasers," *Applied Physics Letters*, 67(19), 2780–2782, 6 November 1995.
- [15] A. Gavrielides, V. Kovanis, P. Varangis, T. Erneux, and T.B. Simpson, "Subharmonic resonances in an optically injected semiconductor laser," *Proceedings SPIE*, 2693, 654–665, 1996.
- [16] S. Piazzolla, P. Spano, and M. Tamburini, "Small signal analysis of frequency chirping in injection-locked semiconductor lasers," *IEEE Journal of Quantum Electronics*, QE-22(12), 2219–2223, December 1986.
- [17] P. Gallion, H. Nakajima, G. Debarge, and C. Chabran, "Contribution of spontaneous emission to the linewidth of an injection-locked semiconductor laser," *Electronics Letters*, 21(14), 626–628, 4 July 1985.
- [18] T.B. Simpson and J.M. Liu, "Enhanced modulation bandwidth in injection-locked semiconductor lasers," *IEEE Photonics Technology Letters*, submitted for publication, 1997.
- [19] F. Mogensen, H. Olesen, and G. Jacobsen, "Locking conditions and stability properties for a semiconductor laser with external light injection," *IEEE Journal of Quantum Electronics*, QE-21(7), 784–793, July 1985.
- [20] R. Hui, A. D'Ottavi, A. Mecozzi, and P. Spano, "Injection locking in distributed feedback semiconductor lasers," *IEEE Journal of Quantum Electronics*, 27(6), 1688–1695, June 1991.
- [21] D. Boggavarapu, J.W. Grantham, Y.Z. Hu, H.M. Gibbs, G. Khitrova, S. Koch, M. Sargent III, and W.W. Chow, "Injection locking of vertical-cavity surface-emitting laser," *Nonlinear Dynamics in Optical Systems Technical Digest, OSA Technical Digest Series*, 16, 281–283, 1992.
- [22] H. Haken, *Synergetics*. Springer-Verlag, Berlin, 1983.
- [23] M. Sargent III, M.O. Scully, and Jr W.E. Lamb, *Laser Physics*. Addison-Wesley, Reading, MA, 1974.
- [24] M. Lax, "The theory of laser noise," *Proceedings SPIE*, 1376, 2–20, 1991.
- [25] R. Hui, S. Benedetto, and I. Montrosset, "Near threshold operation of semiconductor lasers and resonant-type laser amplifiers," *IEEE Journal of Quantum Electronics*, 29(6), 1488–1497, June 1993.
- [26] G. Björk, A. Karlsson, and Y. Yamamoto, "On the linewidth of microcavity lasers," *Applied Physics Letters*, 60(3), 304–306, 20 January 1992.
- [27] K. Vahala and A. Yariv, "Semiclassical theory of noise in semiconductor lasers-part II," *IEEE Journal of Quantum Electronics*, QE-19(6), 1102–1109, June 1983.

REPORT OF INVENTIONS AND SUBCONTRACTS

(Pursuant to "Patent Rights" Contract Clause (See Instructions on Reverse Side)

Public reporting burden for this collection of information is estimated to average 1 hour per response, including the time for reviewing instructions, searching existing data sources, gathering and maintaining the data needed, and completing and reviewing the collection of information. Send comments regarding this burden estimate or any other aspect of this collection of information, including suggestions for reducing this burden to Washington Headquarters Services, Directorate for Information Operations and Reports, 1215 Jefferson Davis Highway, Suite 1204, Arlington, VA 22202-4302, and to the Office of Management and Budget, Paperwork Reduction Project (0000-0959), Washington, DC 20503.

PLEASE DO NOT RETURN YOUR COMPLETED FORM TO EITHER OF THESE ADDRESSES. RETURN COMPLETED FORM TO THE CONTRACTING OFFICER.

1a. NAME OF CONTRACTOR/SUBCONTRACT	2a. NAME OF GOVERNMENT PRIME CONTRACTOR			3. TYPE OF REPORT (X one)
JAYCOR	US ARMY RESEARCH OFFICE			
b. ADDRESS (Include ZIP Code)	d. AWARD DATE (YYMMDD)			4. REPORTING PERIOD (YYMMDD)
P.O. Box 85154 San Diego, CA 92186-5154	96 05 15			a. FROM 96 05 15
c. CONTRACT NUMBER				b. TO 96 11 14

SECTION I - SUBJECT INVENTIONS

5. "SUBJECT INVENTIONS" REQUIRED TO BE REPORTED BY CONTRACTOR/SUBCONTRACTOR (If "None," so state)

a. NAME(S) OF INVENTOR(S) <i>(Last, First, MI)</i>	b. TITLE OF INVENTION(S)	c. DISCLOSURE NO., PATENT APPLICATION SERIAL NO. OR PATENT NO.	d. ELECTION TO FILE PATENT APPLICATION	e. CONFIRMATORY INSTRUMENT OR ASSIGNMENT FORWARDED TO CONTRACTING OFFICER
			(1) United States (a) Yes (b) No	(2) Foreign (a) Yes (b) No
NONE				

f. EMPLOYER OF INVENTOR(S) NOT EMPLOYED BY CONTRACTOR/SUBCONTRACTOR	g. ELECTED FOREIGN COUNTRIES IN WHICH A PATENT APPLICATION WILL BE FILED
(1) (a) Name of Inventor <i>(Last, First, MI)</i>	(1) Title of Invention (2) Foreign Countries of Patent Application
(b) Name of Employer	
(c) Address of Employer <i>(Include Zip Code)</i>	

SECTION II - SUBCONTRACTS (Containing a "Patent Rights" clause)

6. SUBCONTRACTS AWARDED BY CONTRACTOR/SUBCONTRACTOR (If "None," so state)	7. CERTIFICATION OF REPORT BY CONTRACTOR/SUBCONTRACTOR <i>(Not required if</i> <input checked="" type="checkbox"/> <i>Small Business or</i> <input type="checkbox"/> <i>Non-Profit organization.) (X appropriate box)</i>				
a. NAME OF SUBCONTRACTOR(S)	b. ADDRESS <i>(Include ZIP Code)</i>	c. SUBCONTRACT NO.(S)	d. DFAR "PATENT RIGHTS"	e. DESCRIPTION OF WORK TO BE PERFORMED UNDER SUBCONTRACT(S)	f. SUBCONTRACT DATES (YYMMDD)
			(1) Clause Number (2) Date <i>(YYMM)</i>		(1) Award (2) Estimated Completion
NONE					

7. CERTIFICATION OF REPORT BY CONTRACTOR/SUBCONTRACTOR OFFICIAL <i>(Last, First, MI)</i>	<i>a. NAME OF AUTHORIZED CONTRACTOR/SUBCONTRACTOR OFFICIAL (Last, First, MI)</i> Quintero, Sandra	<i>b. TITLE</i> Senior Contracts Administrator	<i>c. I Certify that the reporting party has procedures for prompt identification and timely disclosure of "Subject Inventions," that such procedures have been followed and that all "Subject Inventions" have been reported.</i>
d. SIGNATURE	<i>d. SIGNATURE</i>		
	11 March 1997		
e. DATE SIGNED			

Previous editions are obsolete.

*Form Approved
OMB No. 9000-0095
Expires July 31, 1995*

GENERAL

This form is for use in submitting INTERIM and FINAL invention reports to the Contracting Officer and for use in the prompt notification of the award of subcontracts containing a "Patent Rights" clause. If the form does not afford sufficient space, multiple forms may be used or plain sheets of paper with proper identification of information by Item Number may be attached.

An INTERIM report is due at least every 12 months from the date of contract award and shall include (a) a listing of "Subject inventions" during the reporting period, (b) a certification of compliance with required invention identification and disclosure procedures together with a certification of reporting of all "Subject Inventions," and (c) any required information not previously reported on subcontracts awarded during the reporting period and containing a "Patent Rights" clause.

A FINAL report is due within 6 months if contractor is a small business firm or domestic nonprofit organization and within 3 months for all others after completion of the contract work and shall include (a) a listing of all "Subject Inventions" required by the contract to be reported and (b) any required information not previously reported on subcontracts awarded during the course of or under the contract and containing a "Patent Rights" clause.

While the form may be used for simultaneously reporting inventions and subcontracts, it may also be used for reporting, promptly after award, subcontracts containing a "Patent Rights" clause.

Dates shall be entered where indicated in certain items on this form and shall be entered in four or six digit numbers in the order of year and month (YYMM) or year, month and day (YYMMDD). Example: April 1986 should be entered as 8604 and April 15, 1986 should be entered as 860415.

Item 1a. Self-explanatory.

Item 1b. Self-explanatory.

Item 1c. If "same" as item 2c, so state.

Item 1d. Self-explanatory

Item 2a. If "same" as item 1a, so state.

Item 2b. Self-explanatory.

Item 2c. Procurement Instrument Identification (PII) number of contract (DFAR 4.7003).

Item 2d thru 5e. Self-explanatory

Item 5f. The name and address of the employer of each invention not employed by the contractor or subcontractor is needed because the Government's rights in a reported invention may not be determined solely by the terms of the "Patent Rights" clause in the contract.

Example 1: If an invention is made by a Government employee assigned to work with a contractor, the Government rights in such an invention will be determined under Executive Order 10096.

Example 2: If an invention is made under a contract by joint inventors and one of the inventors is a Government employee, the Government's rights in such an inventor's interest in the invention will also be determined under Executive Order 10096, except where the contractor is a small business or nonprofit organization, in which case the provisions of Section 202(e) of P.L. 96-517 will apply.

Item 5g (1). Self-explanatory.

Item 5g (2). Self-explanatory with the exception that the contractor or subcontractor shall indicate, if known at the time of this report, whether applications will be filed under either the Patent Cooperation Treaty (PCT) or the European Patent Convention (EPC). If such is known, the letters PCT or EPC shall be entered after each listed country.

Item 6a. Self-explanatory

Item 6b. Self-explanatory

Item 6c. Self-explanatory

Item 6d. Patents Rights Clauses are located in FAR 52.227.

Item 6e thru 7b. Self-explanatory.

Item 7c. Certification not required by small business firms and domestic nonprofit organizations.